Infrared spectroscopic techniques applied in ecological studies

Master's thesis
by
Per Samuelsson

Lund Reports on Atomic Physics, LRAP–435
Atomic Physics Division, Lund University
Lund, March, 2011

Contents

Chapter 1

Introduction

The aim of this study is to develop methods for remote classification of migrating birds, primarily utilizing spectroscopic techniques in the mid infrared (MIR) region, supported by laboratory measurements. Our key approach is to investigate if the temporal modulation of MIR spectral features could be used for possible species identification at night. The concept is presented in Fig. 1.1, and the proposed method is described in greater detail in subsequent chapters.

Studying migration routes of birds is of great ecological interest in itself, and may also give insight into the spread of bird-borne viruses such as avian flu and malaria, and various tick-borne diseases. Migrants generally migrate at high altitudes during night-time, when wind conditions are less turbulent, and they run a smaller risk of falling victim to birds of prey, and these facts define the basic requirements for any detection system. Existing methods for bird detection include tracking radar and infrared imaging, as well as less automated methods, such as lunar obscuration. Tracking radar suffers from the problem that the strength of the return echo depends on the wavelength of the illuminating radiation with respect to the body size of the bird, which means that the latter cannot be determined unambiguously using a fixed wavelength system. IR imaging based methods are mainly used for resolving wing beats, and no information about distance is gained. In order to circumvent these limitations, multimodal systems incorporating both radar and IR imaging have further been used [1]. In this project, this idea is extended to include spectroscopic methods, and the feasibility of remote bird sensing using complementary techniques such as laser-induced fluorescence (LIF) light detection and ranging (lidar), IR imaging, depolarization and passive spectroscopy has been evaluated.

The Lund mobile lidar system is described in detail in [2], and LIF lidar in this context (bird studies) refers to the utilization of pulsed deep UV light (266 nm, corresponding to the fourth harmonic of a Nd:YAG laser) to remotely excite bird plumage, and the detection of the subsequently emitted fluorescence, as filtered through the plumage. The fluorescence is detected by photomultiplier tubes (PMT:s) in three different spectral bands covering the wavelength region from about 300 nm to 570 nm. In

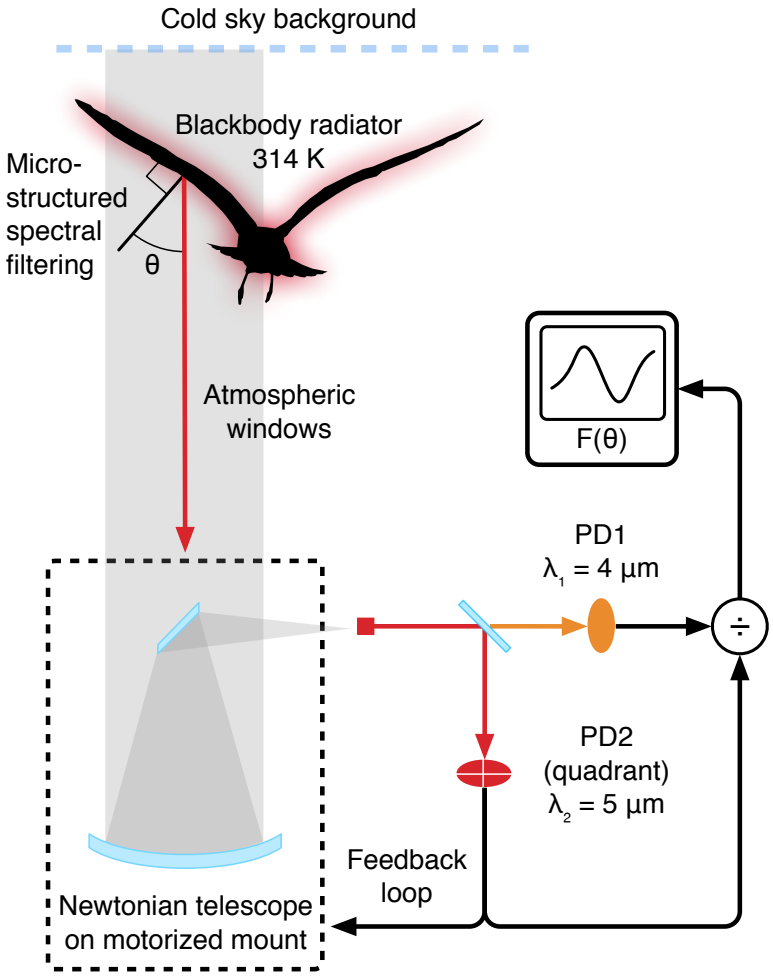

Fig. 1.1. Blackbody radiation is emitted from the bird and filtered through the plumage. Due to wing beating, and angular dependence in the transmittance of the feathers, the ratio between the detected intensities in two spectral bands gives rise to an oscillating signal in time.

addition, the elastically reflected 266 nm light is detected in a fourth band. The effective repetition rate is 10 pulses per second, and a motor-controlled folding mirror preceding a 40 cm diameter Newtonian telescope is used both for directing the illuminating radiation and the detection of the return echo. In addition to LIF lidar, polarization lidar has been attempted, specifically the measurement of the level of depolarization in bird plumage. The present diploma thesis focuses on our work performed in the MIR, however, while other techniques used in our group are covered in more depth in [3].

A means of remote classification must fulfill a number of criteria: the chosen method must be robust, i.e. it should be independent of measurement conditions such as illumination, measurement geometry, instrument response, or that each change to the setup would require recalibration, as well as independent of individual differences such as the sizes of the birds. This is generally accomplished by measuring unitless quantities, e.g., by observing the ratio between the intensity of light incident on a sample to the fraction that is reflected or transmitted, or, in our case, the relative intensity of the emitted fluorescence in three spectral bands. Fluorescence in bird plumage is described in detail in [4], and the transmittance of down in, e.g., [5]. In the present study a new method is proposed which relies on differential transmittance properties of bird plumage in the infrared region.

High specificity is obviously desired in any application involving classification, but the combination of IR signature with other techniques such as LIF lidar etc. relaxes this requirement. A complete system would likely comprise both tracking lidar, IR, and possibly radar, where each such subsystem may give a likelihood for a bird to belong to a given species. Combined with expert knowledge, no isolated subsystem needs to be able to unambiguously classify a bird by itself, but classification is instead based on the joint probability, comprising information from all subsystems. In any case, features must be identified that differentiate different species of interest, or at least different groups of species. Such information may include spectroscopic information as well as expert knowledge such as the size, speed, altitude of the bird, or geographical location. Laboratory measurements show that there are species-dependent differences in how plumage transmits and reflects radiation with regard to angular dependence, and polarization [3]. The spectral transmittance obviously depends on factors such as density and concentration of various pigments, but also angle of incidence and observation, and polarization, which means that not only chemical composition, but also the structure at a larger scale, of the feather determines its optical properties.

Non-invasiveness is another desirable requirement. All passive methods obviously fulfill this requirement, and assuming a suitable wavelength range is used (below about 330 nm for birds due to avian corneal transmission),

this would also include active optical methods such as LIF lidar. The optical properties of bird plumage have been studied in the UV and optical regime (see, e.g., [6] for some early work), corresponding to avian vision, but little attention has been given to its properties beyond the near infrared, and such information may prove to be a valuable complement to other data. Migration birds migrate at altitudes up to 10 km. The atmosphere has three optical windows in the MIR and TIR (thermal infrared) region, at 3–4 µm, around 5 µm and 8–14 µm (see Fig. 3.1), and any ground based remote analysis would have to take this into account.

Finally, cost, both in terms of equipment and operation, is always a consideration if an IR-based system is to be implemented, where passive methods are favorable. The infrared is attractive because a broad-band mid IR source is readily available (in the body metabolism of the bird), and the relative lack of other MIR sources in the sky.

Chapter 2

Background

In the visual range, plumage colors usually arise from a combination of differential absorption by chromophores as well as structural colors, meaning that the reflectance spectrum not only depends on chemical composition of the feathers but also the spatial distribution of the feather structure, at a level of scale that is of the same order of magnitude as the wavelength of the light. Thin-film interference, coherent scattering, diffraction gratings and Bragg reflection are common models used to describe the interaction process, as well as Rayleigh and Mie scattering. The interfaces between structures of different refractive index will give rise to Fresnel reflections, and depending on the level of order in the structures (sheets, fibers, or spherical particles), some spatial frequencies may be enhanced and others suppressed due to constructive and destructive interference of scattered waves. This process is augmented by the fact that the scatterers themselves may constitute pigments such as melanins or carotenoids. When the spatial variation of index of refraction is not spherically symmetric, the material may exhibit iridescence, i.e. the reflectance (and thus transmittance) will be a function of angle of observation and illumination, which is encountered in many biological structures apart from bird plumage.

In order to understand how electromagnetic radiation in a given wavelength region is affected when transmitted through bird plumage, it is necessary to have a sense of scale of the structures involved, their organization, and dielectric properties. An anatomical sketch of a bird feather is shown in Fig. 2.1. In order of decreasing size, a wing feather consists of a central base (rachis), from which extends two rows of barbs. Along opposite side of each barb rows of anterior and posterior barbules attach. The barbules in turn loosely attach to each other by hooklets (barbicels). Barbules have a thickness in the order of 2 µm, and are partially overlapping so that they form a laminar structure which constitutes the majority of the surface area of the feather; see Fig. 2.2. Chemically, feathers consist of β-keratin (with an optical refractive index of $n_{\text{keratin}} \approx 1.56$ to 1.58 [7]), which provides the structural framework, and pigments such as eumelanin (producing black and dark brown hues in the visual), phaeomelanins (red-brown, orange), carotenoids (red, orange, and yellow) and others. Melanin

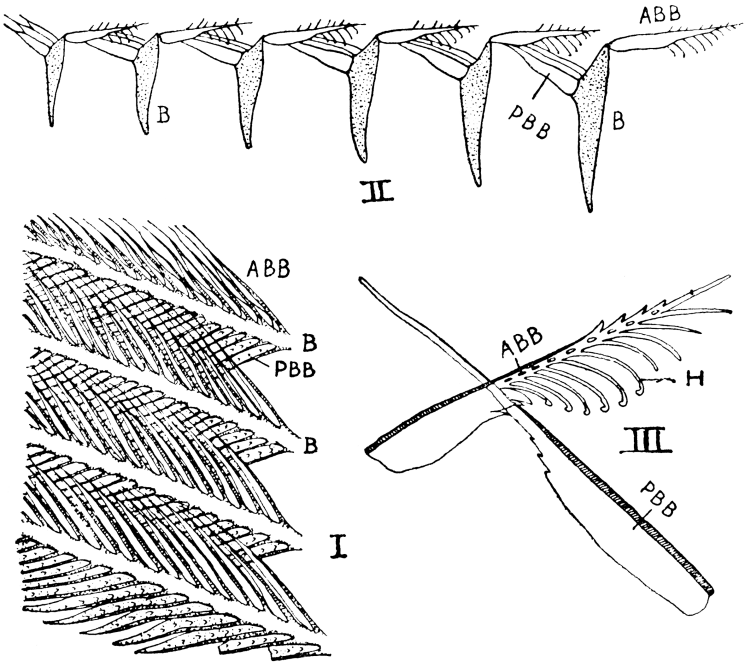

Fig. 2.1. Description: "Parts of a feather. I., Four barbs (B.) bearing anterior barbules (A.BB.) and posterior barbules (P.BB.); II., six barbs (B.) in section, showing interlocking of barbules; III., anterior barbule with barbicels (H.)." Adapted from Thomson, J.A., 1916.

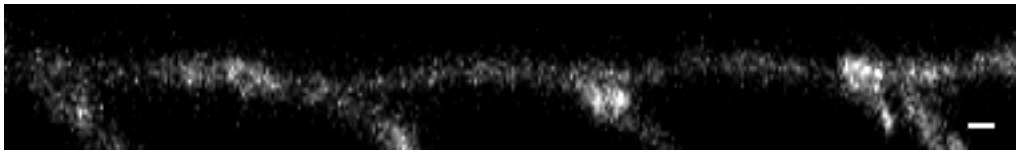

Fig. 2.2. Fluorescence image taken by the author of transverse cross section of overlapping posterior barbules of a herring gull feather. Scale bar measures 2 µm. Imaged using confocal microscopy with laser excitation at 405 nm wavelength, filter cut-off at 420 nm.

($n_{\text{melanin}} \approx 2.0$ [7]) deposits are suspended in the keratin matrix in the form of rod-shaped or spherical granules in a highly ordered way, which may in turn contain air-filled vacuoles, further increasing the gradient of index of refraction, resulting in a reflectance of 11 % at melanin-air interfaces.

According to the Bragg reflection condition, to first order, light with wavelength λ in a medium is scattered an angle θ if there exists spatial variation d in the refractive index whose magnitude is given by $2d\sin(\theta/2) = \lambda$, with minimum $d = \lambda/2$ for $\theta = \pi$. In other words, spatial frequencies d will result in backscattering for wavelengths longer than $2d$. More generally, the density variations can instead be described by a statistical distribution of spatial frequencies, i.e. the Fourier transform [8]. This approach has been applied in a number of cases to predict the reflectance spectra of insects and birds, where the refractive indices were estimated from transmission electron micrographs of the structures [9, 10]. In particular, coherent scattering from spherical structures with sizes in the order of 200 nm have been known to give rise to a reflectance spectrum peaking around 400 nm wavelength [11].

Barbules have a thickness of about 2 µm, which means that, according to the above argument, a reflectance peak can be expected around 4 µm (with higher-order peaks at $2\,\mu\text{m}, 4/3\,\mu\text{m}, 1\,\mu\text{m}, \ldots$). Since the spatial variation is an order of magnitude larger than the visual case, optical microscopy can be employed. Clearly, this does not provide any direct estimate of variation of density (as β-keratin itself is practically transparent to light at optical wavelengths, although highly scattering due to a refractive index of around 1.6); this is merely used as a statistical measure of the mean spatial periodicity of barbules. The position of individual spatial frequency peaks can still be expected to correlate to the frequencies of interest, however. Further, posterior barbules are organized somewhat like Venetian blinds (see Fig. 2.2), implying that even for normally incident light, there will still be photon transport laterally in the feather, perpendicular to barbules, that will experience a frequency component of the spatial variation in refractive index proportional to barbule spatial frequency (see also Fig. 6.3 on page 44).

Chapter 3

Theory

3.1 Thermal radiation

The spectral radiance of an object is defined as the power of radiation emitted per surface area, solid angle and wavelength. A blackbody is a perfect radiator, absorbing all incoming radiation at all wavelengths and emits radiation according to Planck's law,

$$L(\lambda, T) = \frac{2hc^2}{\lambda^5}\left[\exp\left(\frac{hc}{\lambda kT}\right) - 1\right]^{-1}, \tag{3.1}$$

where λ is the wavelength, T is the absolute temperature, h is Planck's constant, c is the speed of light and k is Boltzmann's constant. The Wien displacement law,

$$\lambda = \frac{b}{T}, \qquad b \approx 2\,897\,\mu\mathrm{m\,K}, \tag{3.2}$$

in turn gives the wavelength of maximum radiance for a blackbody at a given temperature T.

The ratio between the spectral radiance of an object and that of a blackbody is given by its emissivity, which is generally wavelength-dependent. Kirchhoff's law of thermal radiation states that, for an object at thermal equilibrium, the emissivity of the object equals its absorptivity, defined as the ratio of the power absorbed to the power of the radiation incident on the object.

Within an atmospheric window, where absorption is low, emission from the sky will thereby also be low, reducing background radiation further (cf. Fig. 3.1). In Fig. 3.2, the spectral radiation of a blackbody has been plotted for a number of temperatures. The effective temperature of the sky is about 281 K [12], and migration birds would have a body temperature a few Kelvin above that of a human (310 K).

3.2 Kramers-Kronig relations

The Kramers-Kronig relations connects the real part $n(\omega)$ of the index of refraction to the imaginary part $\kappa(\omega)$ – and thus the absorption coefficient

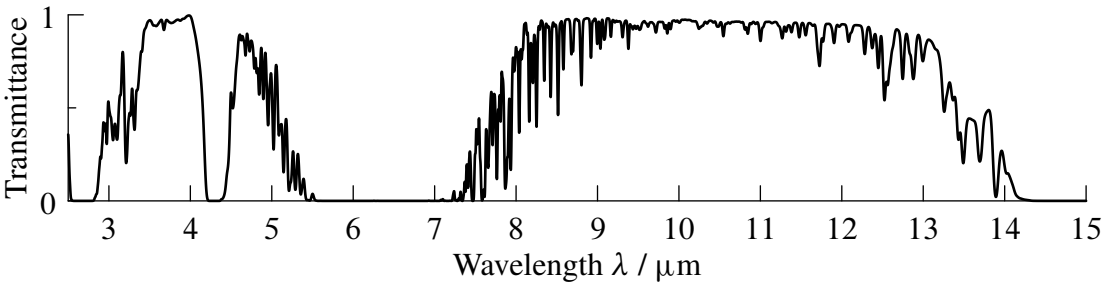

Fig. 3.1. Spectral transmittance of 1 km of vertical standard atmosphere. CO_2 absorption peaks at 2.7 µm, at 4.3 µm and around 14 µm, while water vapor causes the absorption band between 5.5 µm and 7 µm, and is also responsible for the irregularities around 3 µm. Result of simulation based on HITRAN line data (`http://www.cfa.harvard.edu/HITRAN/`).

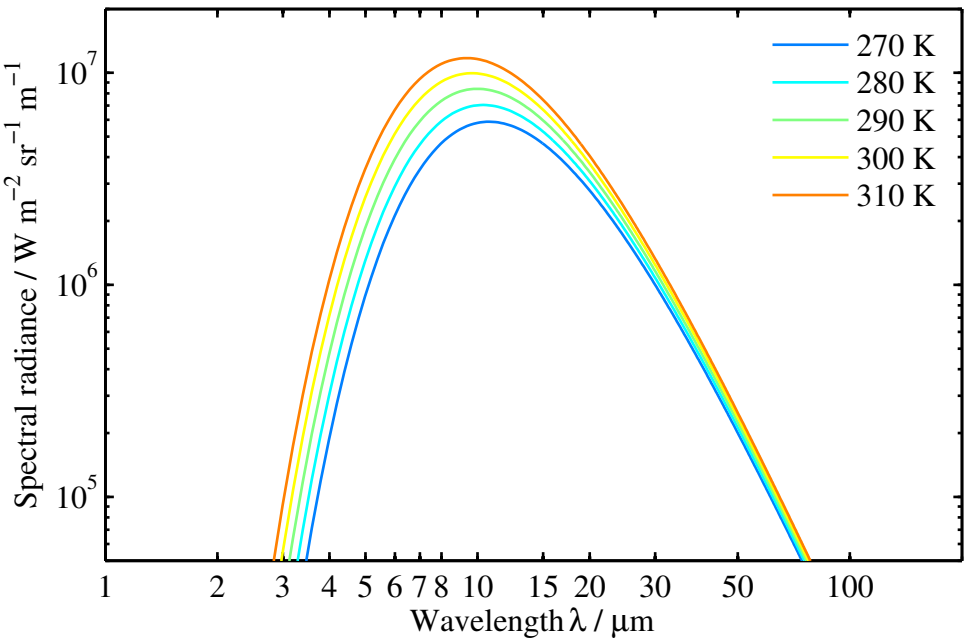

Fig. 3.2. Spectral radiance $L(\lambda, T)$ of a blackbody at different temperatures T. Specifically, for a blackbody at $T = 310\,\mathrm{K}$, $L(\lambda)$ peaks at $\lambda \approx 9.35\,\mu\mathrm{m}$. At this temperature, the spectral radiance at 10 µm is three times as high as at 5 µm, and 124 times the spectral radiance at 3 µm.

$\mu_{\mathrm{a}}(\omega)$ – through the equations

$$n(\omega) = 1 + \frac{2}{\pi}\mathcal{P}\int_0^\infty \frac{\omega'\kappa(\omega')}{\omega'^2 - \omega^2}\,d\omega', \tag{3.3}$$

$$\kappa(\omega) = -\frac{2\omega}{\pi}\mathcal{P}\int_0^\infty \frac{n(\omega') - 1}{\omega'^2 - \omega^2}\,d\omega', \tag{3.4}$$

where $\kappa(\omega) = c\mu_{\mathrm{a}}(\omega)/2\omega$ is the extinction coefficient (see, e.g., [13, Ch. 4]). This inter-dependence is illustrated graphically in Fig. 3.3 (top two curves). If one is known for all wavelengths, or can be approximated reliably, the other can be calculated: if the path length is known, the absorption coefficient may be determined using the Beer-Lambert law from trans-illumination measurements; and the refractive index, e.g., from reflectance measurements and the Fresnel equations.

3.3 Christiansen effect

When transparent particles of refractive index n_1 are immersed in a medium with a refractive index n_2, and n_1 or n_2 is varied so that they coincide, the volume will become optically homogeneous, negating losses due to scattering, and increasing the collimated transmittance. This is achieved by, e.g., dilution of the immersion substance, or naturally, due to the wavelength dependence of the indices of refraction, allowing for determination of one index of refraction if the other is known. However, close to an absorption band, the wavelength of maximum transmittance will not exactly correspond to the wavelengths where $n_1 = n_2$, as illustrated in Fig. 3.3. In addition, phase shifts due to differences in indices of refraction will influence the total attenuation coefficient and therefore the transmittance, discussed further in [14].

A further application of the Christiansen effect is within the field of atmospheric science, allowing essentially for seeing through clouds or aerosols in a narrow spectral band close to an absorption line; see, e.g., [15, 16].

3.4 Scattering

Structural colors in biological structures are commonly caused by coherent scattering, i.e., scattering of of light by particles inside tissue that have some level of spatial ordering with regard to each other. This may be seen as a weaker form of Bragg diffraction, where each atom has a well-defined position in a crystal lattice. This is as opposed to pure Rayleigh or Mie scattering, where scatterers are assumed to be acting individually.

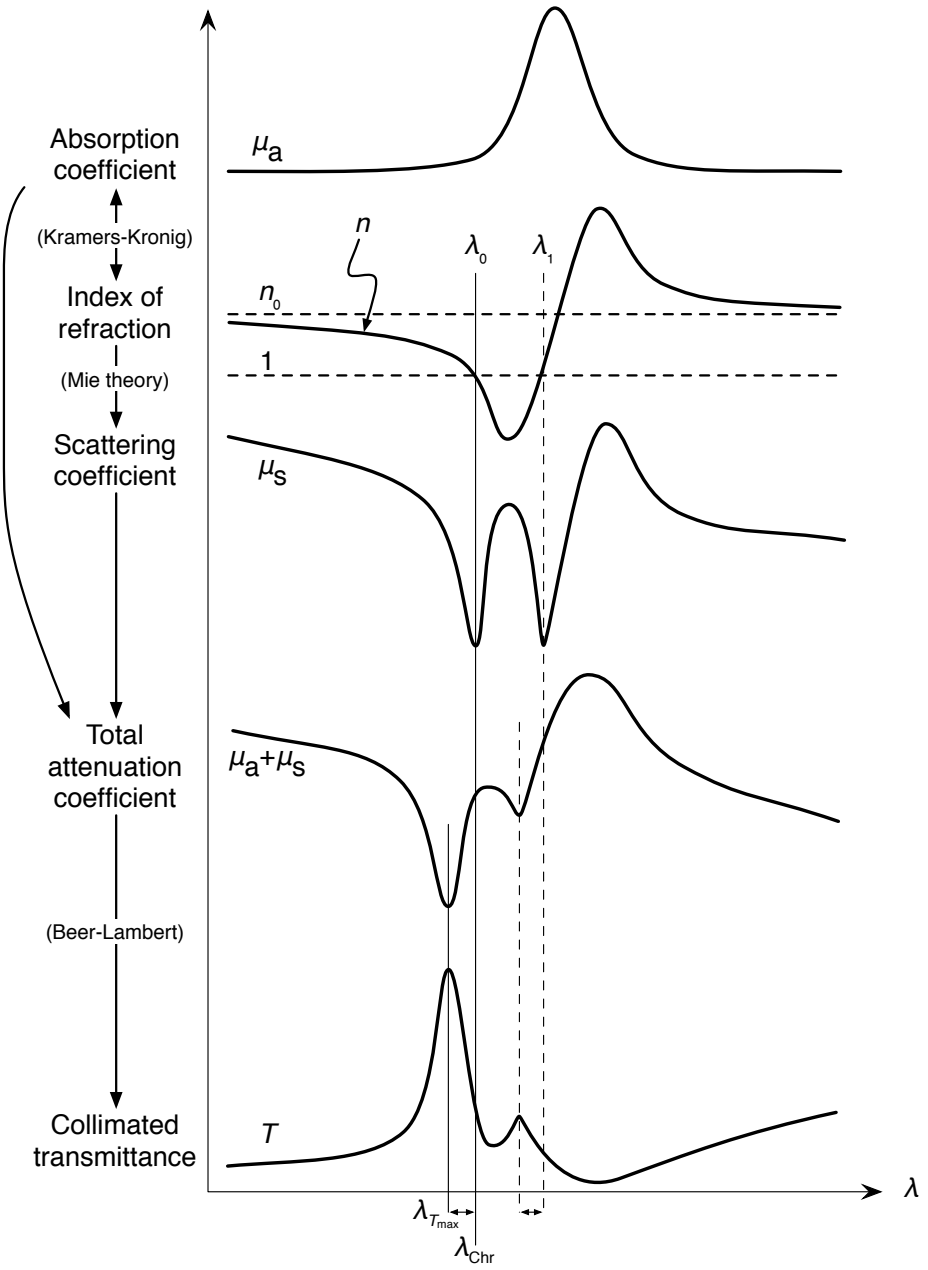

Fig. 3.3. Christiansen effect in a medium consisting of keratin (refractive index n, $n_0 \approx 1.6$) and air. Due to the Kramers-Kronig relations, a peak in the absorption spectrum will result in a dip in refractive index n at slightly shorter wavelength. This causes n to become 1, negating attenuation due to scattering at the wavelengths λ_0 and λ_1. The total attenuation is given by $\mu_a + \mu_s$. Since λ_0 and λ_1 are located on the positive flank of the absorption peak, the resulting peaks in the transmittance spectrum will be shifted slightly with regard to λ_0 and λ_1, towards shorter wavelengths.

3.5 Thin-film optics

From previous work by others, in the optical regime, thin-film interference has been used to predict the reflectance spectrum of iridescent feathers, so this model is a natural starting point for the present study in the MIR. Thin-film interference refers to the interference between the monochromatic light reflected off the front and back surfaces of the film. If if this model can be used as an approximation to describe the layers of barbules, the wavelength of the transmission peak depends on the angle of incidence θ relative to the optical surface normal of the film according to

$$\lambda_\theta = \lambda_0 \frac{\sqrt{n^2 - \sin^2\theta}}{n},$$

where λ_0 is the wavelength of the peak at normal incidence, and n is the effective index of refraction. That is, for increasing angles of incidence, the peak will shift towards shorter wavelengths.

3.6 Fourier transform spectroscopy

A conceptual drawing of a Fourier transform spectrometer is shown in Fig. 3.4. The incoming wave with intensity I_0 is separated by a semi-transparent mirror M_1 (reflectivity $\mathcal{R}_1 = 50\,\%$), and reflected off the mirrors M_2 ($\mathcal{R}_2 = 100\,\%$) and M_3 ($\mathcal{R}_3 = 100\,\%$), the latter being scannable along the beam. (In the instrument, these are actually corner-cube reflectors.) The difference in path length x between the two arms M_1–M_2 and M_1–M_3 introduces a corresponding phase shift. Half the intensity from each beam

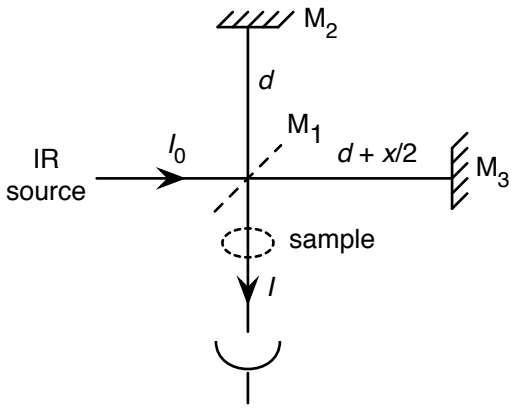

Fig. 3.4. Fourier transform spectrometer beam paths

ends up being reflected back at the source; the remainder is absorbed and scattered by the sample. Without any sample, the complex amplitude of a plane wave after the interferometer, at a point x_0 is therefore

$$A(k,x) = \frac{\sqrt{I_0}}{2}\exp[-ik(x_0+x)] + \frac{\sqrt{I_0}}{2}\exp(-ikx_0),$$

where x is the difference in path length, and k is the wavenumber. Choosing $x_0 = 0$ at the detector, we have the intensity for a narrow frequency range

$$I(k,x) = |A(k,x)|^2 = \frac{I_0}{4}|\exp(-ikx)+1|^2 = \frac{I_0}{2}[1+\cos(kx)].$$

Introducing a sample with spectral transmittance $\mathcal{T}(k)$ in the beam, and integrating over all frequencies gives the total intensity at the detector,

$$\begin{aligned} I(x) &= \int_0^\infty \mathcal{T}(k) I(k,x)\, dk \\ &= \frac{I_0}{2}\int_0^\infty \mathcal{T}(k)\, dk + \frac{I_0}{2}\int_0^\infty \mathcal{T}(k)\cos(kx)\, dk. \end{aligned}$$

The first term can be recognized as the intensity at zero displacement, i.e.

$$\frac{2}{I_0}\left[I(x) - \frac{1}{2}I(x=0)\right] = \int_0^\infty \mathcal{T}(k)\cos(kx)\, dk.$$

The right hand expression can be identified as the inverse Fourier transform of $\mathcal{T}(k)$,

$$\frac{2}{I_0}\left[I(x) - \frac{1}{2}I(x=0)\right] = \mathcal{F}^{-1}\mathcal{T}(k),$$

which shows that the transmittance $\mathcal{T}(k)$ can be obtained by the Fourier transform of the detected intensity $I(x)$ with the zero-displacement intensity $I(0)$ subtracted:

$$\mathcal{T}(k) = \frac{2}{I_0}\mathcal{F}\left[I(x) - \frac{1}{2}I(x=0)\right],$$

if the upper integration limit is truncated at some finite displacement x. Spectral emission curve of the IR source, spectral responsivity of the detector and transmittance and reflectivity of atmosphere and optics have been ignored above, and are in practice compensated for by dividing the signal with a dark spectrum recorded with no sample present.

Chapter 4

Method

4.1 FTIR measurements

The transmittance of feathers from a number of different museum specimens of birds (see Table 4.1) were measured using FTIR, as a function of angle of incidence. The feathers were mounted in slide frames and fixed to a rotation mount, and the transmittance measured using an FTIR spectrometer (ATI Mattson model Infinity AR60). To prevent light leakage when the feather did not cover the entire frame, cardboard masks were used, with rectangular apertures with sizes ranging from $1\,\mathrm{cm} \times 1\,\mathrm{cm}$ to $1.5\,\mathrm{cm} \times 2.5\,\mathrm{cm}$, depending on the size of the feather. The feathers were then rotated around the central base in increments of 5°, between −50° and 50° angle of incidence, where 0° is normal to the feather surface. The transmittance was measured in a collimation mode, which means that light that is not transmitted or forward scattered, is not detected, and the absorption profile cannot be directly inferred from the transmittance spectra. A background spectrum was taken at the start of each angular sequence, and transmittance was measured at each increment between 2.5 µm and 25 µm with an energy resolution of $0.96\,\mathrm{cm}^{-1}$. Each spectrum was taken as the average of 64 scans.

The polarization state of the beam before and after passing the sample is

Table 4.1. List of bird feathers used in the study

English name (Swe. name)	Latin name
Blackbird (koltrast)	*Turdus merula*
Pallid harrier (stäpphök)	*Circus macrourus*
Herring gull (gråtrut)	*Larus argentatus*
Sparrowhawk (sparvhök)	*Accipiter nisus*
Scarlet ibis (röd ibis)	*Eudocimus ruber*
Chattering lory (gulmantellori)	*Lorius garrulus*
European roller (blåkråka)	*Coracias garrulus*
Rook (råka)	*Corvus frugilegus*
Turaco (turako)	*Tauraco porphyreolophus*

unknown as no polarizer working in the MIR was available. β-barium borate (BBO) transmission cuts off around 3 µm, which makes, e.g., Glan prisms in this material unusable in the MIR. YVO_4 polarizing prisms may be used up to 4 µm, and wire-grid polarizers wherever the substrate transmits, making them the preferable choice.

The wavelength $\lambda_{\mathcal{T}_{\max}}$ of peak feather transmittance was determined in the MIR, by fitting a a 6:th order polynomial to each spectrum in the region 3.6–5.4 µm, and $\lambda_{\mathcal{T}_{\max}}$ was determined from the fit.

An attempt to make reflectance measurements was made, but due to insufficient intensity reaching detector, the resulting spectra were extremely noisy, and are not presented here. However, it can be expected that the dips in the reflectance spectrum would shift along with the transmission peaks.

4.2 Microscopy

For comparison to the transmittance measurements, microscope images of the feathers, still fixed in their frames, were taken using a Brunel microscopes Ltd. model SP80, connected to an AVT Guppy-503 B/C CMOS camera, with 810 nm LED illumination in transmission mode.

A live histogram was used to optimize the dynamic range for each feather; the camera gain, integration time and LED power were adjusted in order not to under- or over-expose the detector. For this reason, the intensity of the images cannot be compared directly.

Initial measurements using a confocal microscope (Zeiss) were also attempted, in order to obtain depth resolved information about the variation in refractive index of the feathers. Restrictions with regard to maximum allowed sample size meant that a small part of the feather had to be cut out, which may have resulted in structural alterations in the keratin matrix, possibly made worse by the immersion of the feather in index matching liquid. The sample was illuminated by 405 nm light, with a filter blocking wavelengths below 420 nm. A single herring gull feather was analyzed in this way, and the resulting fluorescence image is shown in Fig. 2.2.

4.3 Spatial frequency analysis

As mentioned previously, the barbules constitute the majority of the surface area of the feather, and due to their thickness, and spatial organization, they are likely responsible for the observed effects in the MIR. For this reason, the microscope images were analyzed using the spatial Fourier transform.

To measure the barbule periodicity reliably, two different approaches were employed. The most realistic case, the two-dimensional Fourier transform was computed for a set of micrographs. Each Fourier spectrum was taken as an ensemble average of several sub-images, which were each weighted by a Blackman window [17], in order to reduce variance and suppress side lobes. The result was then transformed to polar coordinates (r, θ), and integrated along the radial axis (with the zero frequency component in the origin), which gives the total Fourier power as a function of angle $\theta \in [0, \pi)$. By weighting the spectrum in the frequency interval that is expected to encompass the spatial barbule periodicity (10–40 µm), the peak detection could be improved. The angles perpendicular to barbules on opposite sides of the barbs were then located by finding the angles of peak Fourier power. Computing the two-dimensional Fourier transform along these directions, and integrating along the transverse direction produces an effective parametrization of the original image. The baseline of the resulting (1-dimensional) Fourier spectrum was subtracted, and the barbule period for each direction were determined as the maximum value of the Fourier spectrum in the spatial frequency interval corresponding to spatial periods $T_\theta \in [10\,\mu\text{m}, 40\,\mu\text{m}]$.

The one-dimensional Fourier transform was also computed parallel to and along either side of the barb, and scaled along the spatial axis to account for the difference in angles between barbs and barbule. While exhibiting less noise and more well-defined peaks, it may on the other hand not be representative of the feather as a whole.

To compare the transmittance measurements to the barbule spatial frequencies obtained from the microscopy, singular value decomposition (SVD) of the spectra was employed. A training set for the spatial frequencies was obtained using a linear regression model and leave-one-out cross validation. This entails predicting the spatial periodicity for each feather, using a linear model based on all SVD components and the periodicities for every feather in the set but the one being predicted. The resulting predictions are then validated against the measured values and the process is repeated for different levels of truncation of the number of components included in the model.

4.4 IR imaging

Photomultiplier tubes (PMT:s) are generally not available at the wavelengths of interest, with IR photons having energy below the threshold for photoelectric effect. Instead, possibly cooled, semiconductor detectors may be used. Figure 4.1 shows the normalized detector responsivity of three different detector materials, as well as the spectral transmittance of three

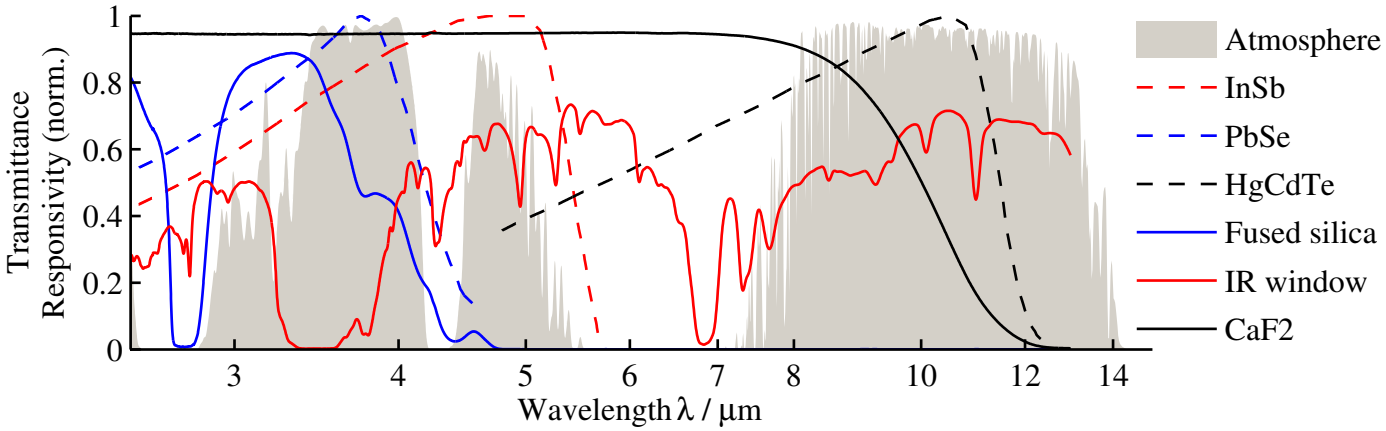

Fig. 4.1. Transmittance (solid lines) and normalized responsivity (dashed lines) of optical filters and detectors, respectively, in the MIR. Note, the responsivity of HgCdTe is determined by the ratio of CdTe (with a bandgap of 1.5 eV corresponding to about 830 nm) to HgTe (zero bandgap). Responsivity profiles adapted from [18].

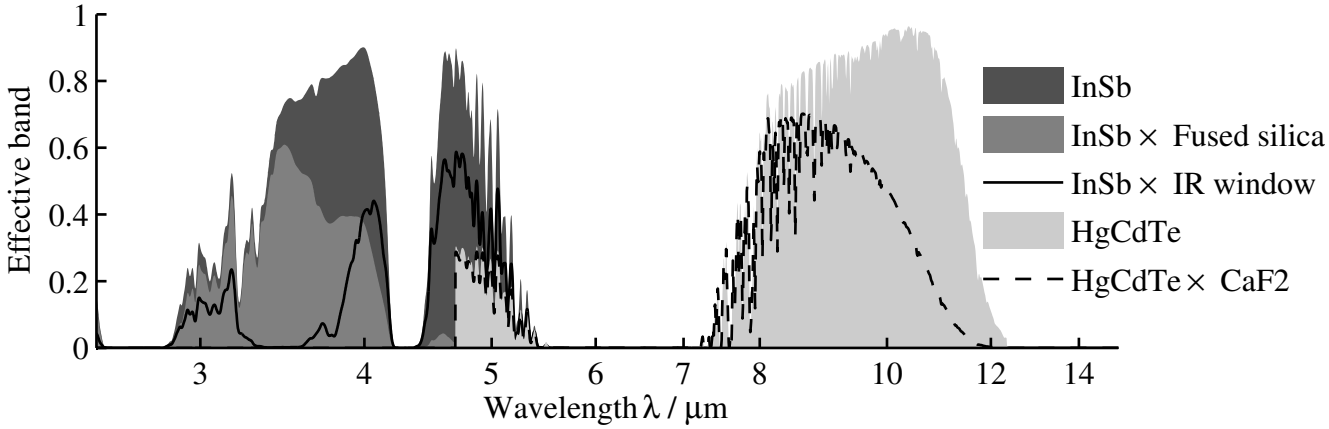

Fig. 4.2. Effective spectral bands for a few filter–detector combinations and atmospheric transmission from Fig. 4.1.

filter materials that may be used for spectral band selection. In Fig. 4.2 the corresponding effective spectral bands are shown.

While a dedicated system would likely employ point detectors with two different spectral bands connected to a telescope (see Fig. 1.1), for evaluation purposes, imaging detectors are convenient. In this project, an AGEMA ThermoVision 900 SW (InSb, LN_2 cooled, sensitive 2–5.6 µm) and a ThermoVision 900 LW (HgCdTe, Stirling cooled, 8–12 µm) scanning thermal cameras were employed, configured to output the raw detector signal as opposed to temperature (corrected in software for nonlinearities due to

optics). Dual band detection is made possible by an image divider, originally designed for gas correlation imaging, that can be fitted to either camera, allowing different filters to be used for each band [19]. The effective bands achieved in this way are displayed in Fig. 4.2. The frame rate is selectable between 15 Hz and 30 Hz, with half the number of scan lines.

On 2010–11–30 (clear sky, −8 °C), measurements were performed on in-vivo Zebra finches. The birds were hand-held against the sky, while the wing-beats were imaged using the dual-band setup in the MIR and TIR (see Fig. 4.2; no IR window was used), at a range of about 5 m. Due to the low frame rate of the IR cameras (15–30 Hz), a visual camera (Basler model Pilot, frame rate up to 210 Hz), was used for reference. IR data were recorded using FLIR ThermaCam Researcher software running on a laptop, connected to the cameras via an AGEMA Camera 900 parallel interface. Visual data was acquired simultaneously on another laptop, running a C++ program that stored the time of each frame in addition to the image itself. Synchronization between the visual and IR streams was made possible by utilization of a trigger signal emitted by Camera 900 each time an IR frame is recorded, driving a LED placed in the FOV of the visual camera (which was not available at the time when the electronics were developed, otherwise this could have been done electrically, as well). Each IR recording session was initiated by an external trigger, and signaled by another LED.

Background images (average of a few frames of only sky) were recorded at the start of each sequence, and subtracted from each image in the sequence, accounting for filter emission. By determining the location of common points in the resulting images of each band, an affine transform can be determined which transforms one image into the coordinate system of the other. The following contrast function was then used to determine the final frame:

$$I = \frac{I_1 - kI_2}{I_1}, \tag{4.1}$$

where I_1 is the image of the band with no filter present, and I_2 is the image with either fused silica or CaF_2 filter, depending on whether the MIR or TIR setup was being used. The constant was chosen as $k = 10$ in the MIR case and $k = 2$ in TIR to account for the relative intensity in each band (see Fig. 4.2 and Fig. 3.2).

In practice, perfect overlapping may be hard to achieve, and any shift will cause edges to have great influence on the resulting ratio image I. A more robust way is to take the average of the pixels of each band image (possibly after background-foreground segmentation, and a slight dilation to account for errors in overlapping), and form the corresponding ratio from the averages, effectively simulating the signal from a point detector. Since

the birds were hand-held out of necessity, and the hand having about the same temperature as the bird itself, separation of hand pixels from bird pixels is somewhat problematic.

The MIR data suffered from prohibitively low SNR, likely due to the relatively low radiance in this wavelength region, since the TIR data were largely unaffected, and the difference in noise levels too great to be attributed to differences in detectivity between the different sensors used.

In-vivo measurements were also performed under laboratory conditions, in-doors. Static in-vivo Zebra finches were imaged by recording up to 50 images sequentially in a single band, then switching to the other band. The resulting images were averaged over an entire sequence to suppress noise, and the background was subtracted.

Chapter 5

Results

5.1 FTIR measurements

Figure 5.1 shows examples of collimated transmittance of feathers, at normal incidence to the feather surface. To aid comparison, the spectra were normalized to the region 2.5 µm–3 µm.

In Figs 5.2–5.10, collimated transmittance was measured under varying angle of incidence, where zero degrees corresponds to normal incidence to the feather surface, and the axis of rotation coincides with the base of the feather. The logarithms of the resulting spectra were normalized to the peak at 5.9 µm, and then transformed back. For a few of the more interesting cases, the peak position is also plotted as a function of angle of incidence, cf. Figs 5.11–5.16. In some cases, the feather was also rotated around an axis perpendicular to the base, in the same plane as the feather (noted in the figure captions).

In Fig. 5.17, the transmittance was measured when a gull feather was stretched, causing the broad peak to shift from 4.17 µm to 4.48 µm.

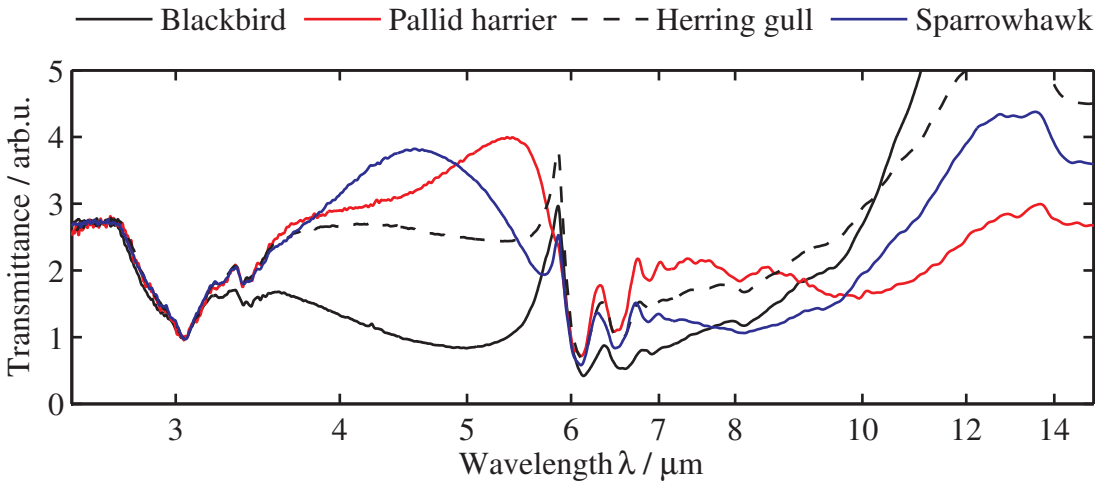

Fig. 5.1. Normalized feather transmittance, at normal incidence

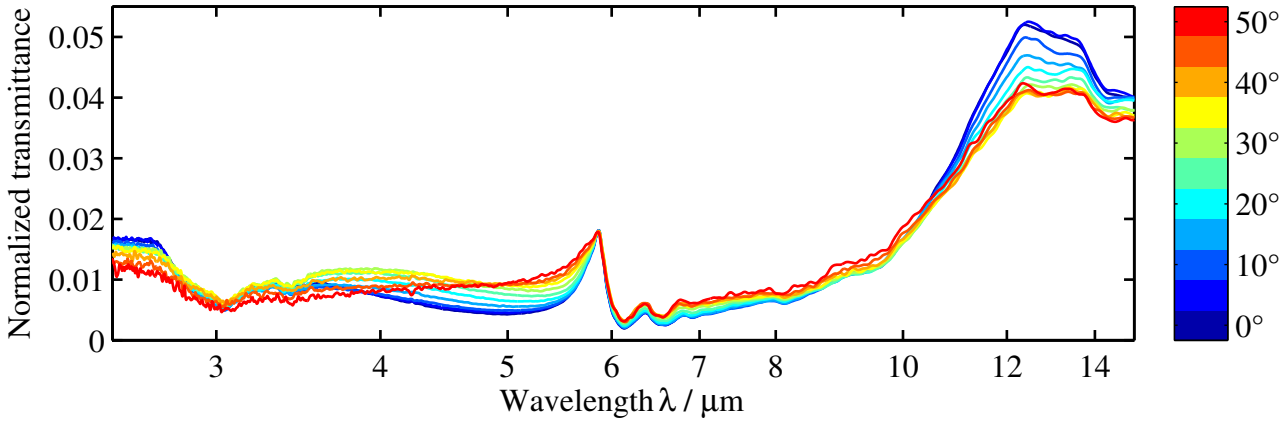

Fig. 5.2. Blackbird feather transmittance as a function of angle of incidence

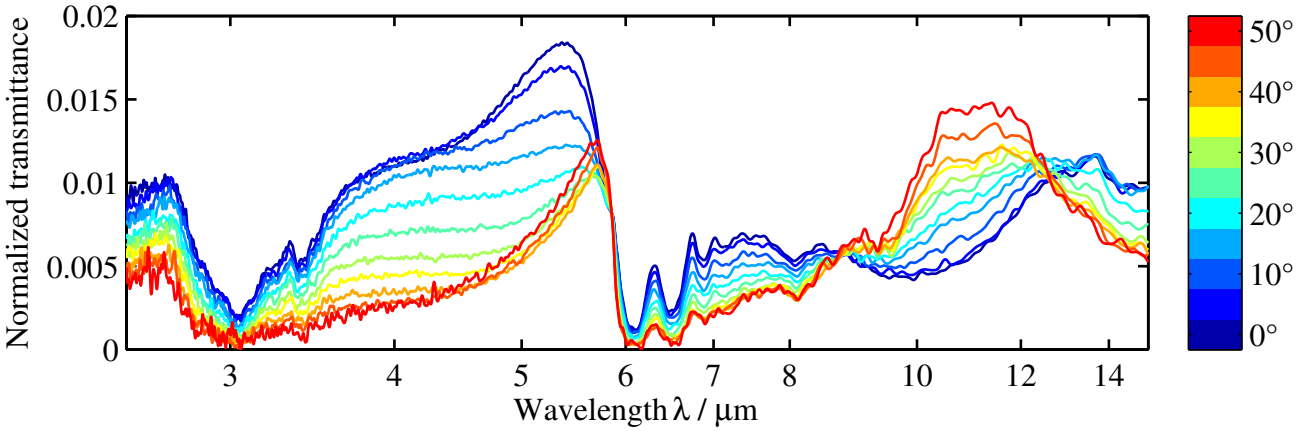

Fig. 5.3. Pallid harrier feather transmittance as a function of angle of incidence

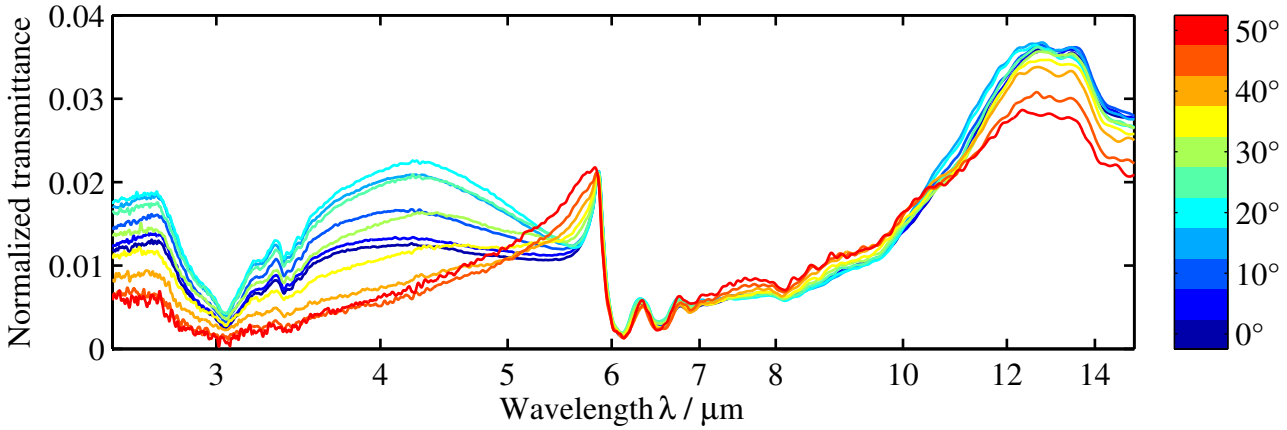

Fig. 5.4. Herring gull feather transmittance as a function of angle of incidence

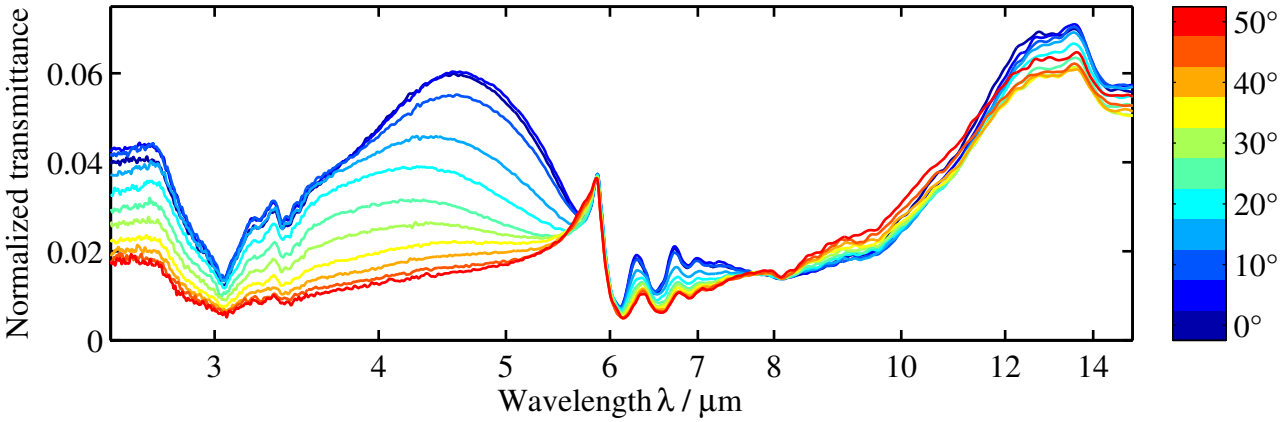

Fig. 5.5. Sparrowhawk feather transmittance as a function of angle of incidence

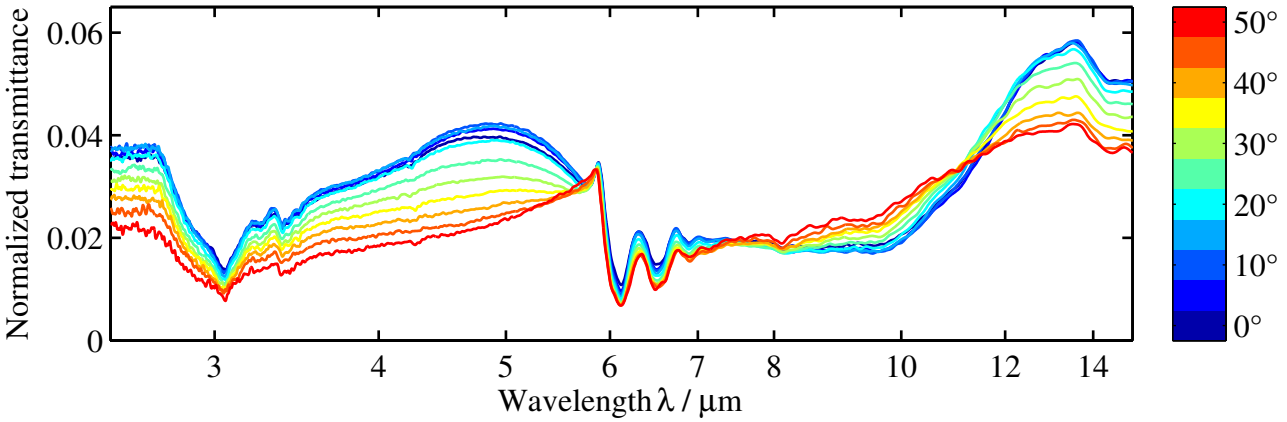

Fig. 5.6. Scarlet ibis feather transmittance as a function of angle of incidence

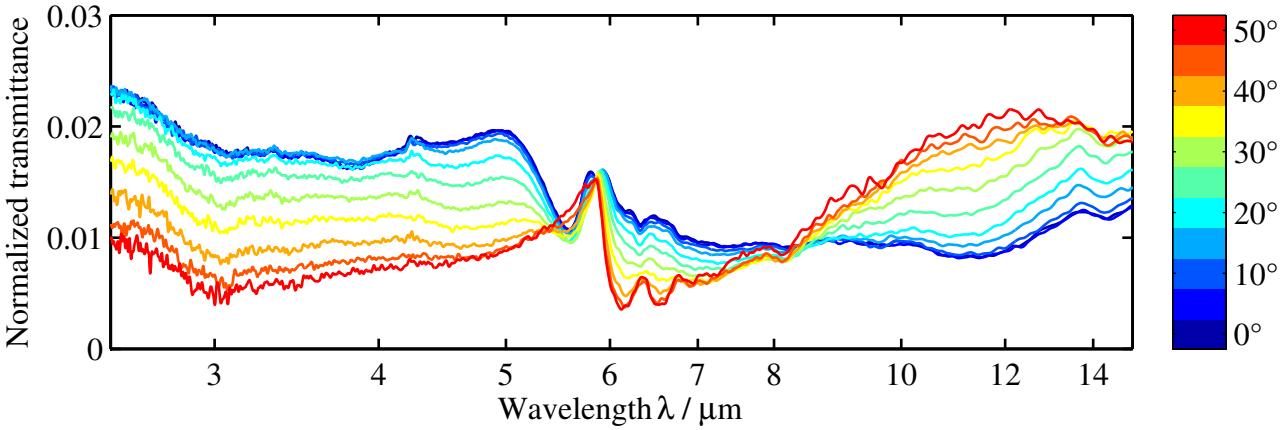

Fig. 5.7. Chattering lory feather transmittance as a function of angle of incidence

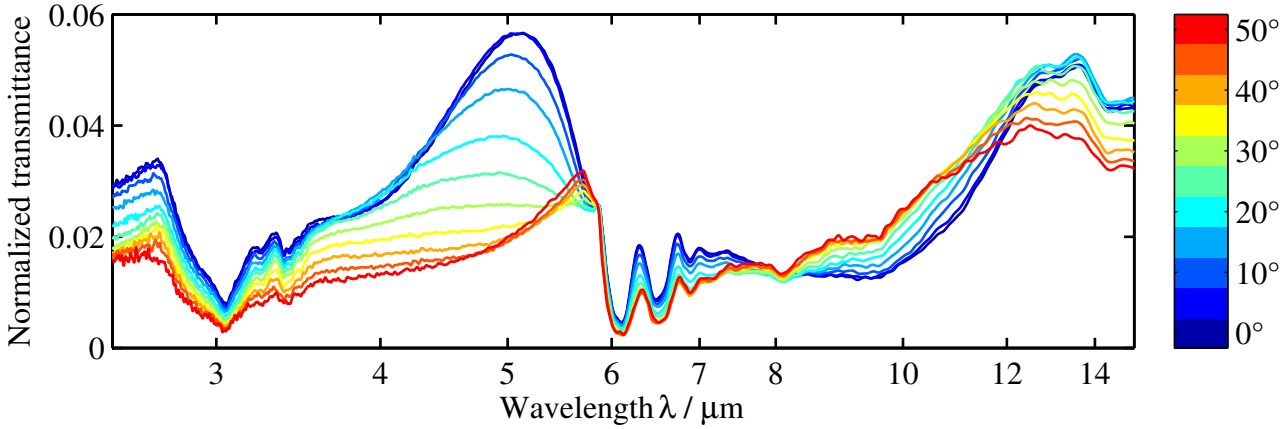

Fig. 5.8. European roller feather transmittance as a function of angle of incidence

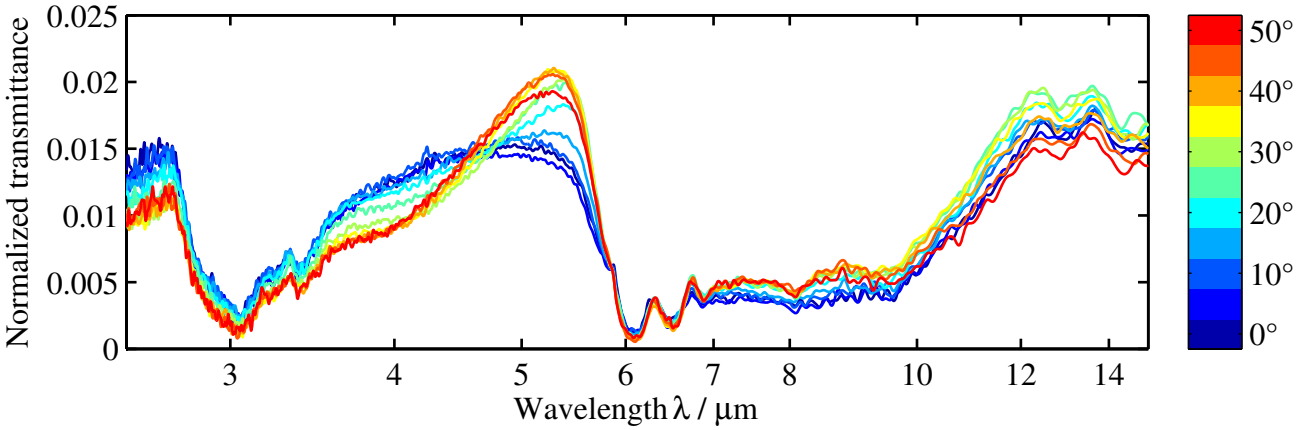

Fig. 5.9. Rook feather transmittance as a function of angle of incidence

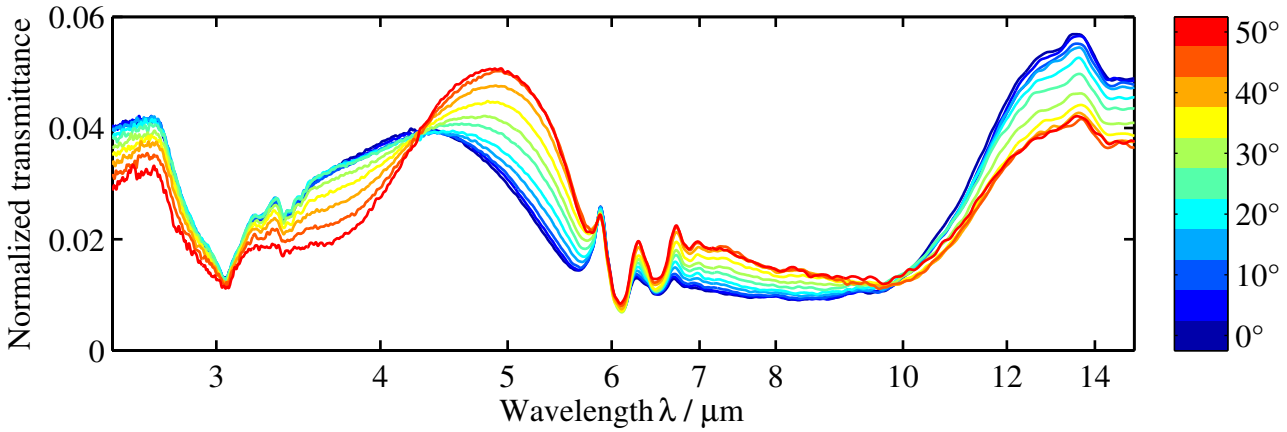

Fig. 5.10. Turaco feather transmittance as a function of angle of incidence

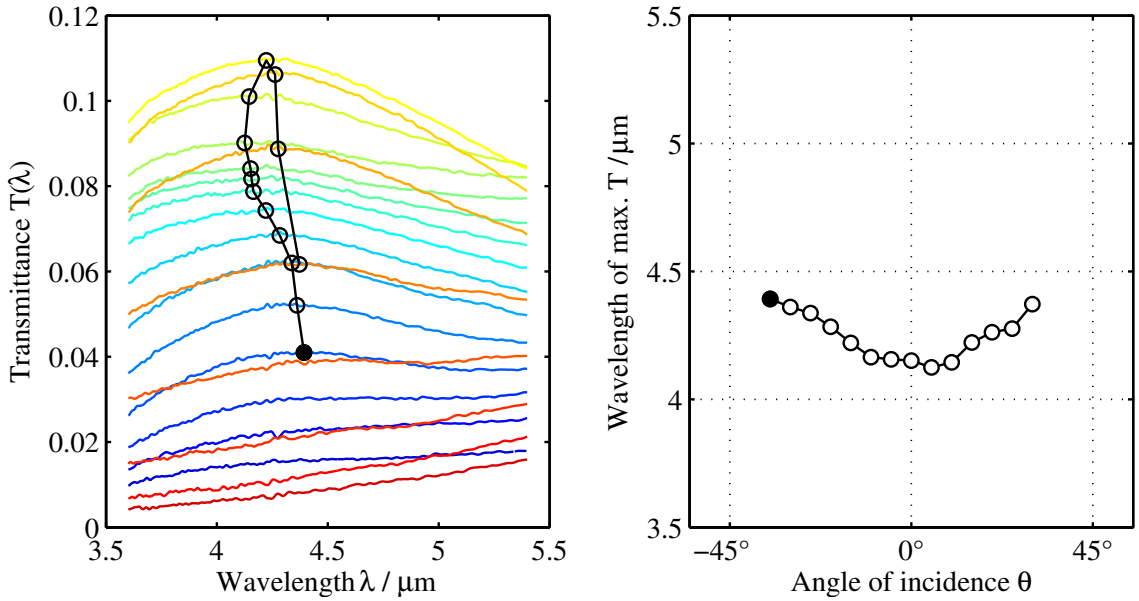

Fig. 5.11. Herring gull feather transmittance as a function of angle of incidence, during rotation around the base

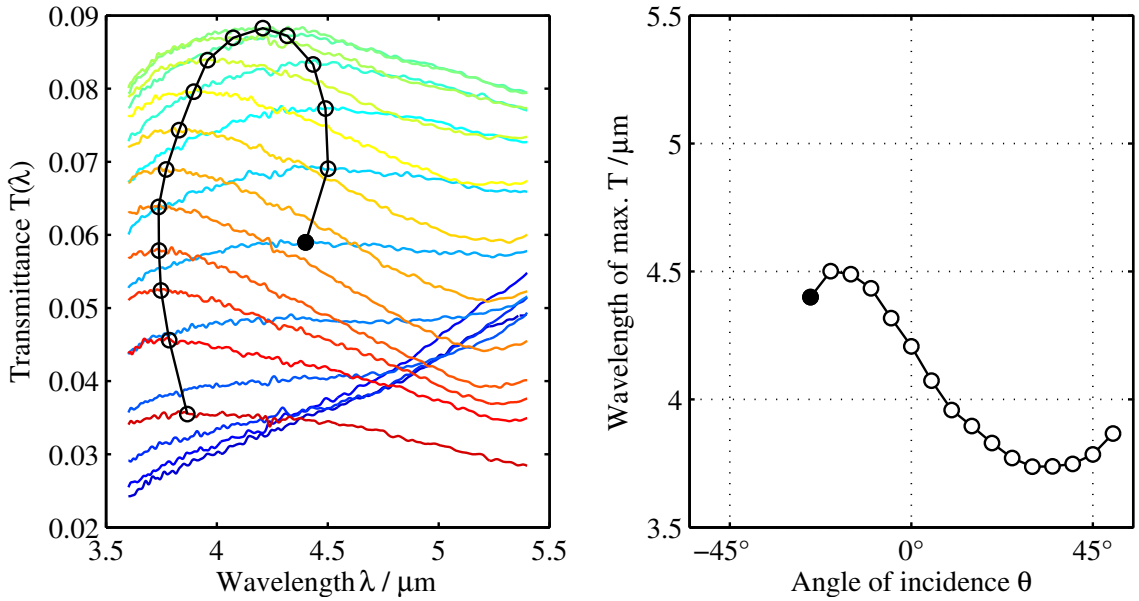

Fig. 5.12. Herring gull feather transmittance as a function of angle of incidence, during rotation about an axis perpendicular to the feather base

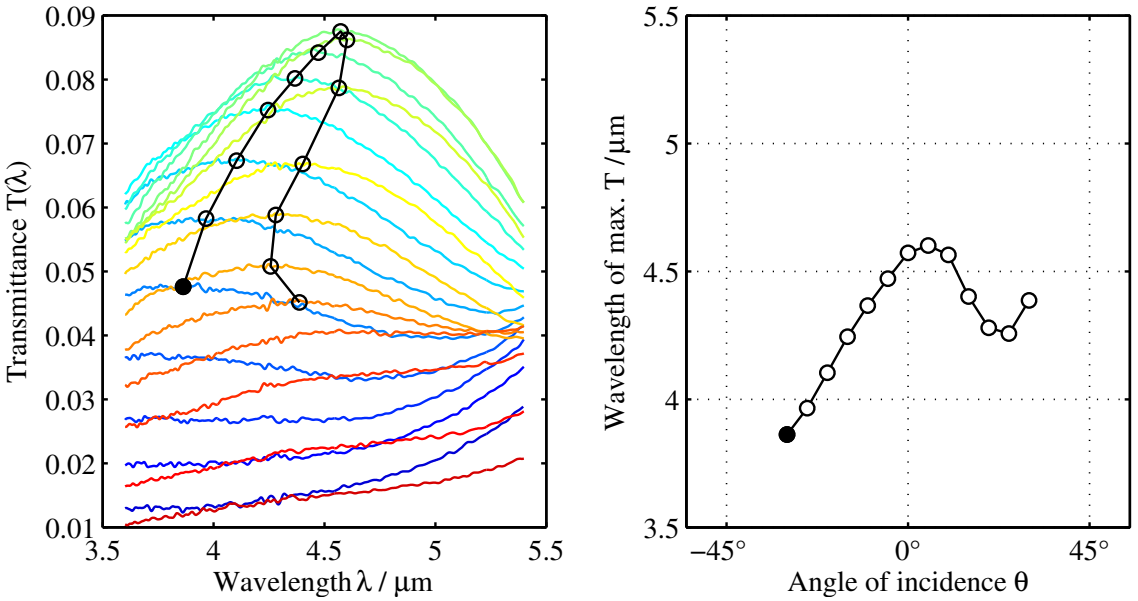

Fig. 5.13. Sparrowhawk feather transmittance as a function of angle of incidence, during rotation around the base

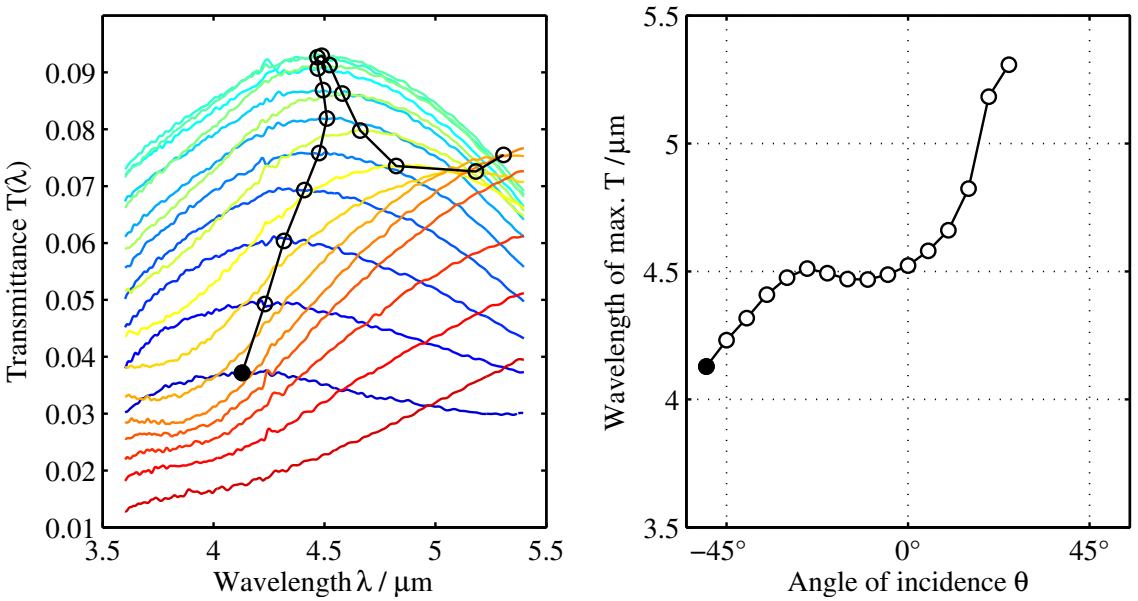

Fig. 5.14. Sparrowhawk feather transmittance as a function of angle of incidence, during rotation about an axis perpendicular to the feather base

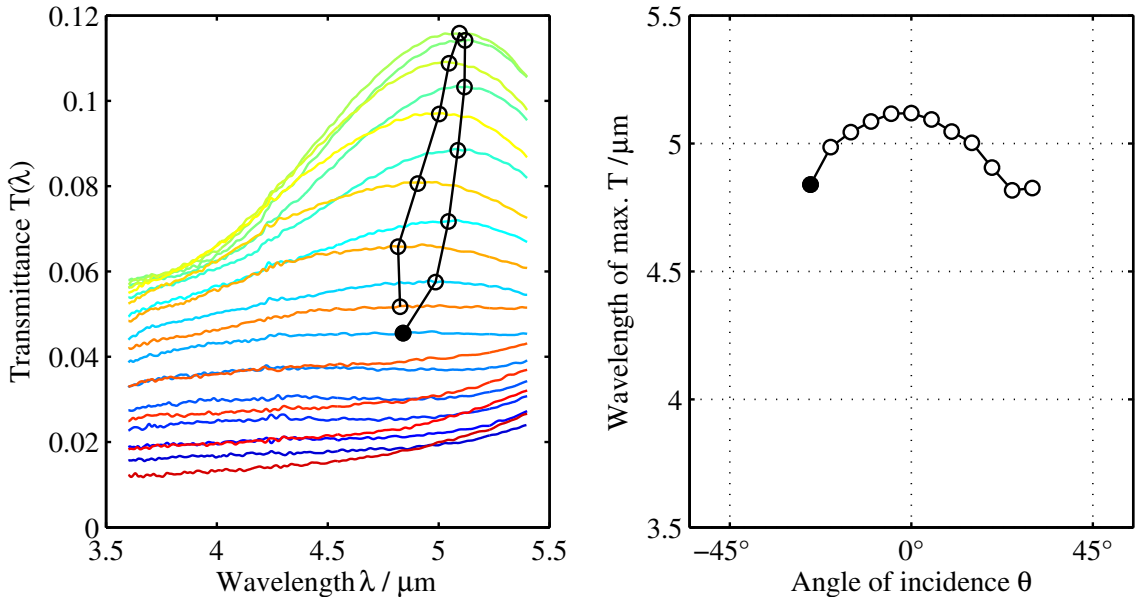

Fig. 5.15. European roller feather transmittance as a function of angle of incidence, during rotation around the base

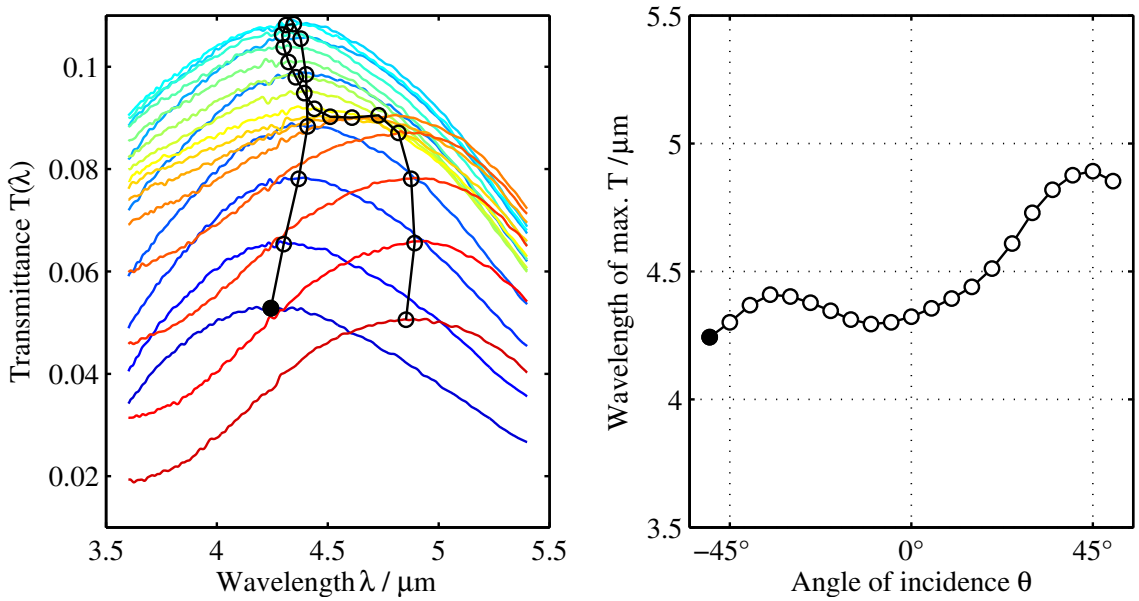

Fig. 5.16. Turaco feather transmittance as a function of angle of incidence, during rotation around the base

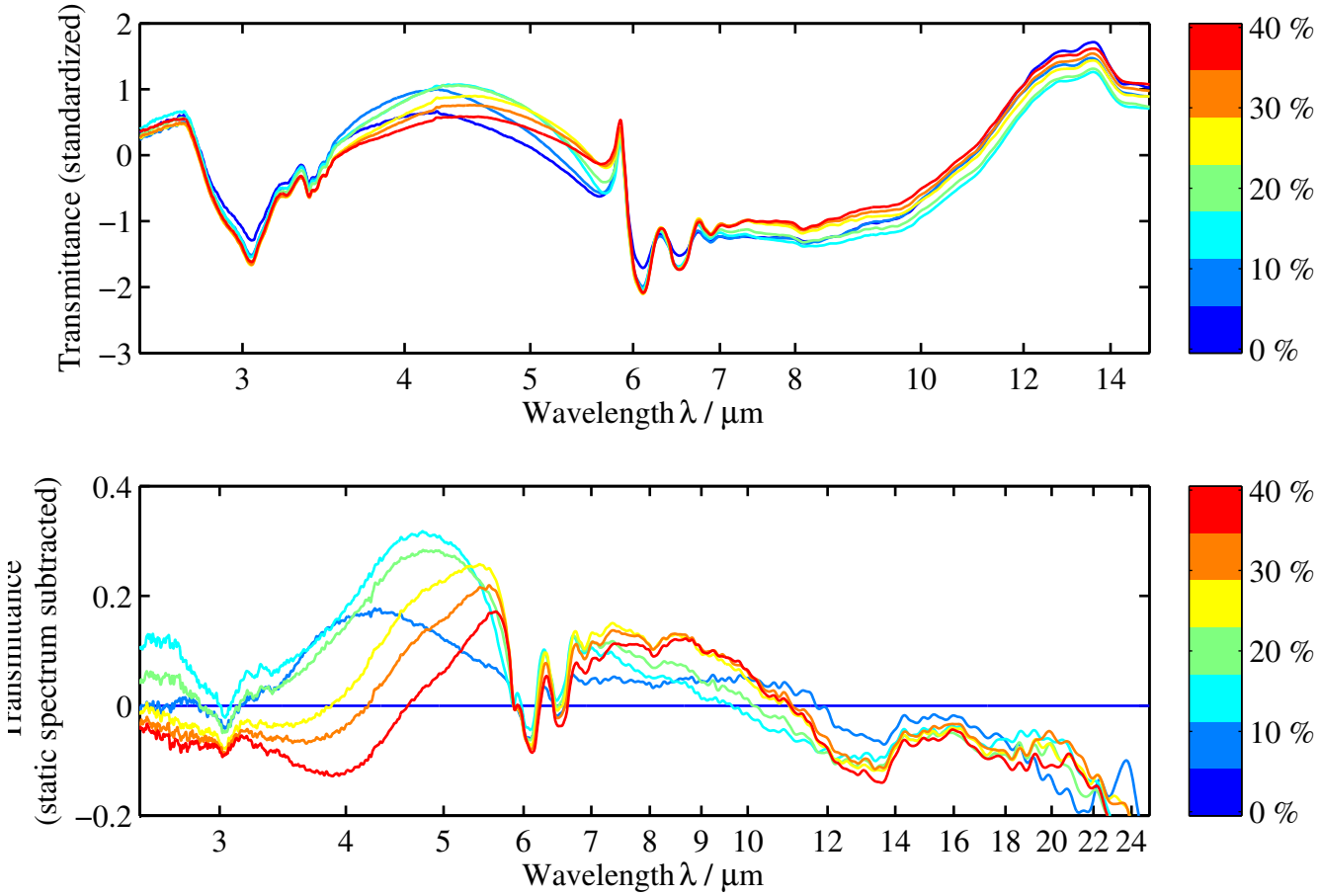

Fig. 5.17. Effect of stretching a herring gull feather on spectral transmittance, resulting in a peak shift from 4.17 µm to 4.48 µm. Top: standardized transmittance; bottom: transmittance spectrum with zero-stretch spectrum subtracted.

5.2 Microscopy and spatial frequency analysis

The results from the feather microscopy and the corresponding Fourier spectra are shown in Figs 5.20–5.28. An overview of the procedure is shown on page 29. A direct comparison of the results from the microscopy and spectroscopic measurements is shown graphically in Fig. 5.29. Cross validation with the herring gull feather excluded from the training and validation sets, yields a correlation coefficient of 95% between the true and predicted spatial periodicities when four SVD components are included, and 83% with two components. If the herring gull feather is included, the corresponding correlation coefficients become 89% and 69%, with four and two components included, respectively; see Figs 5.30 and 5.31.

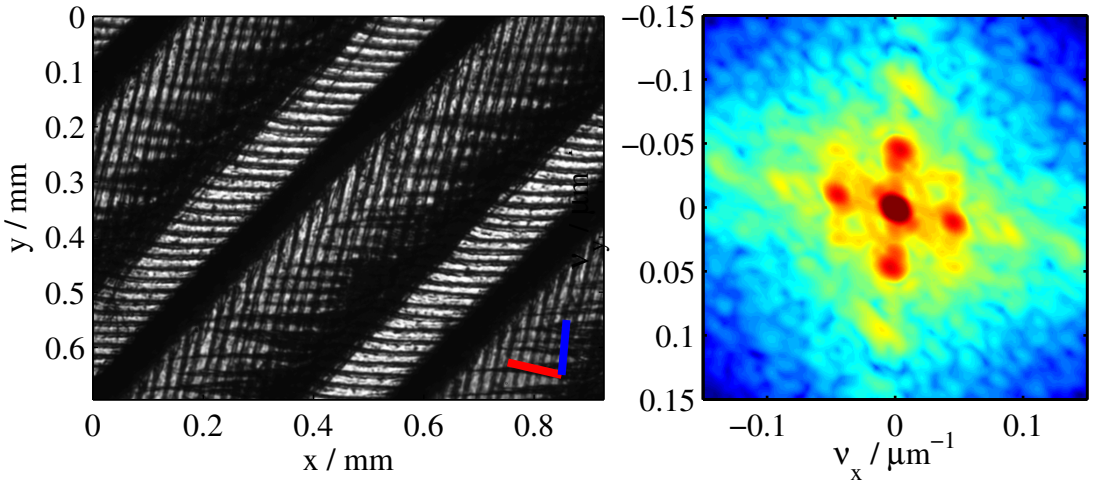

Fig. 5.18. Example microscope image $f(x, y)$ and the (log absolute) of its Fourier transform $(\mathcal{F}f)(\nu_x, \nu_y)$. The base runs horizontally (above visible area, attaches to the right), and barbs run diagonally in the image, from which posterior barbules extend from the upper side and anterior from the lower. The arrows indicate directions θ perpendicular to anterior (red, $\theta = \alpha$) and posterior (blue, $\theta = \beta$) barbules, as determined from Fig. 5.19, along which the presented 1D Fourier spectra were computed.

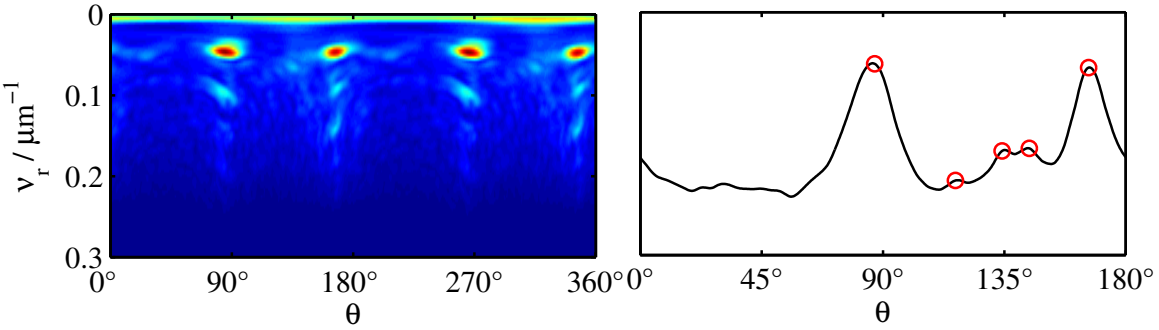

Fig. 5.19. The Fourier spectrum depicted in Fig. 5.18 after polar transformation (left), and integrated along the radial axis (right), which was used for determination of directions θ perpendicular to barbules. Red circles indicate candidates for barbule directions.

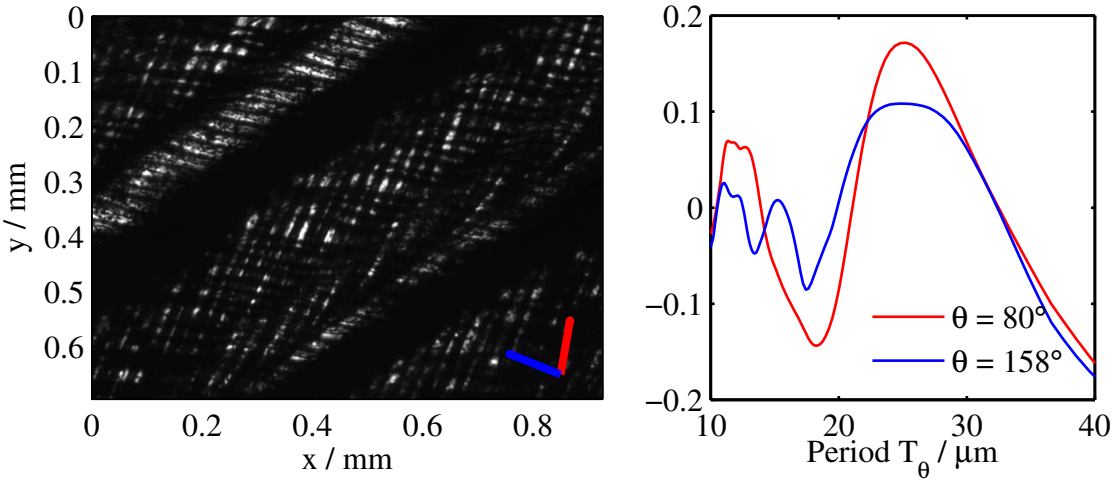

Fig. 5.20. Pallid harrier feather and corresponding Fourier spectra

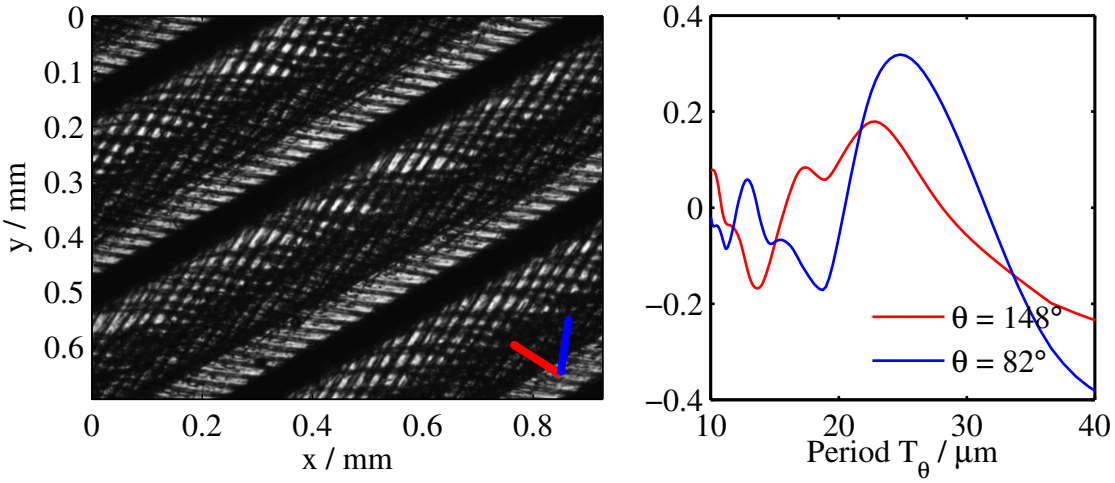

Fig. 5.21. Herring gull feather and corresponding Fourier spectra

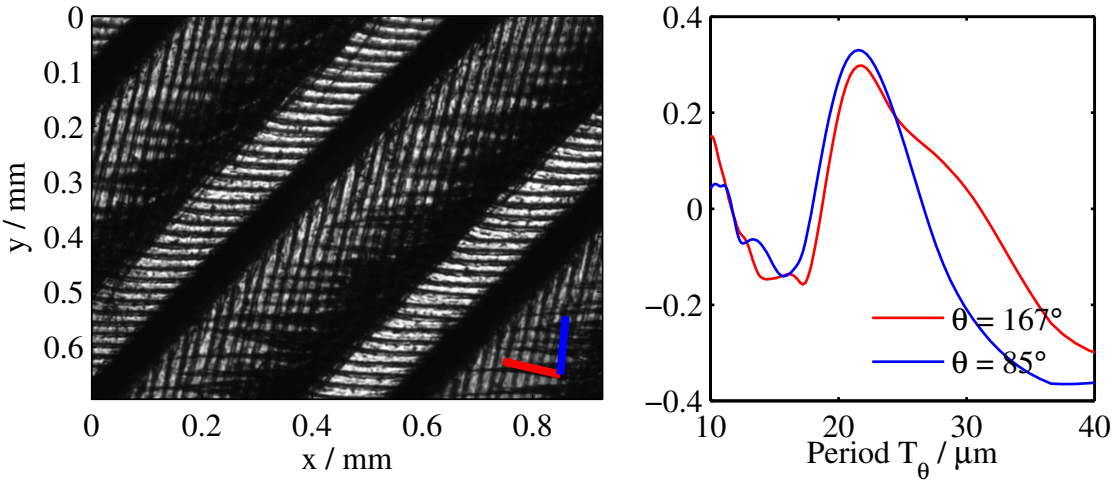

Fig. 5.22. Sparrowhawk feather and corresponding Fourier spectra

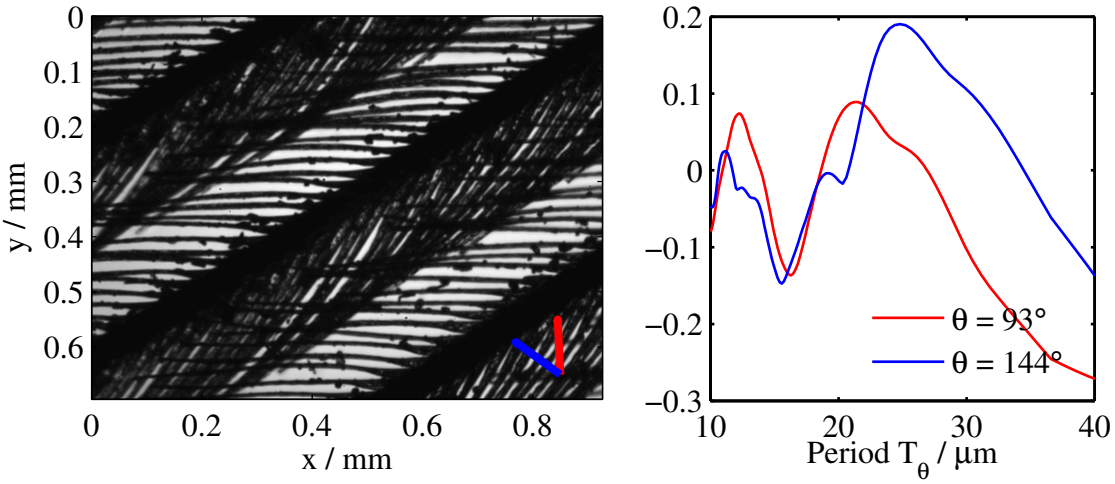

Fig. 5.23. Chattering lory feather and corresponding Fourier spectra

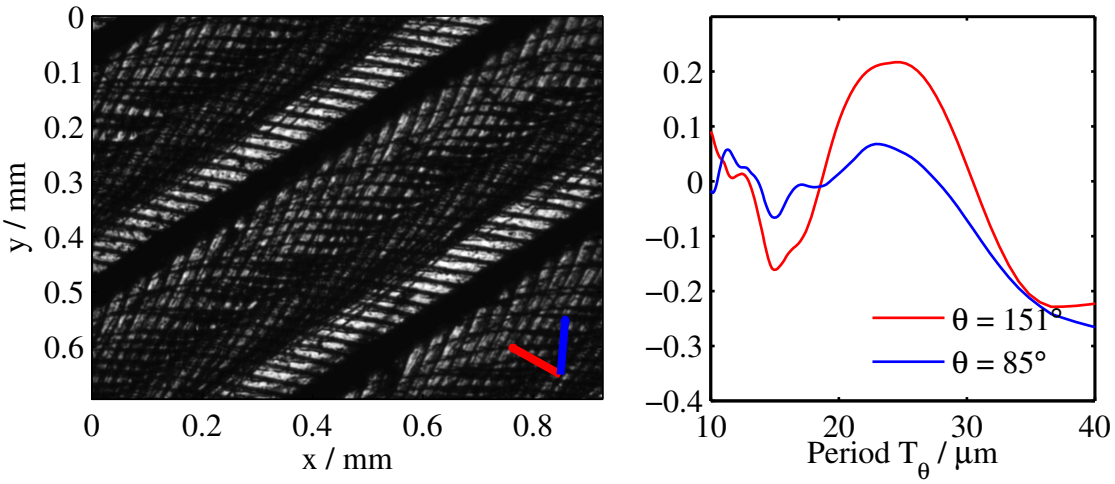

Fig. 5.24. European roller feather and corresponding Fourier spectra

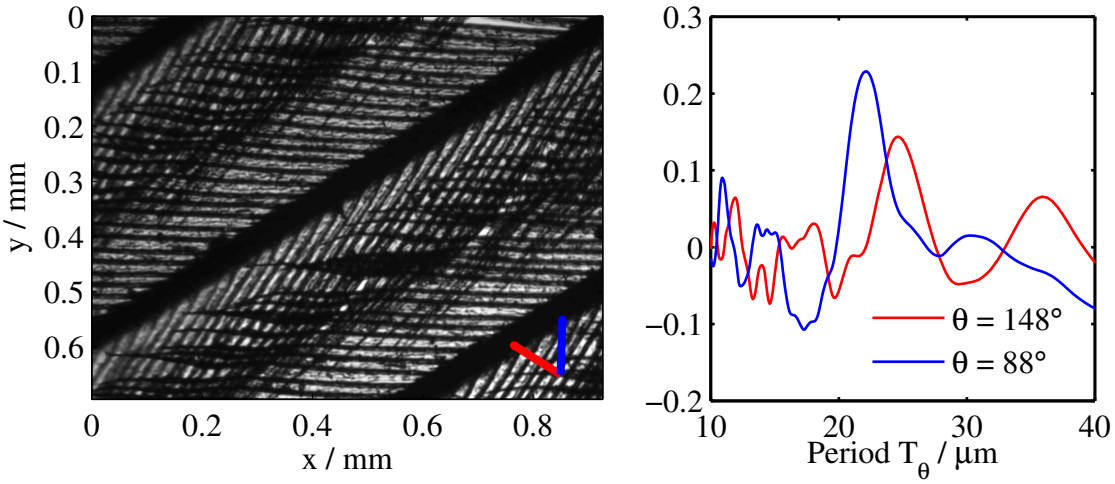

Fig. 5.25. Turaco feather and corresponding Fourier spectra

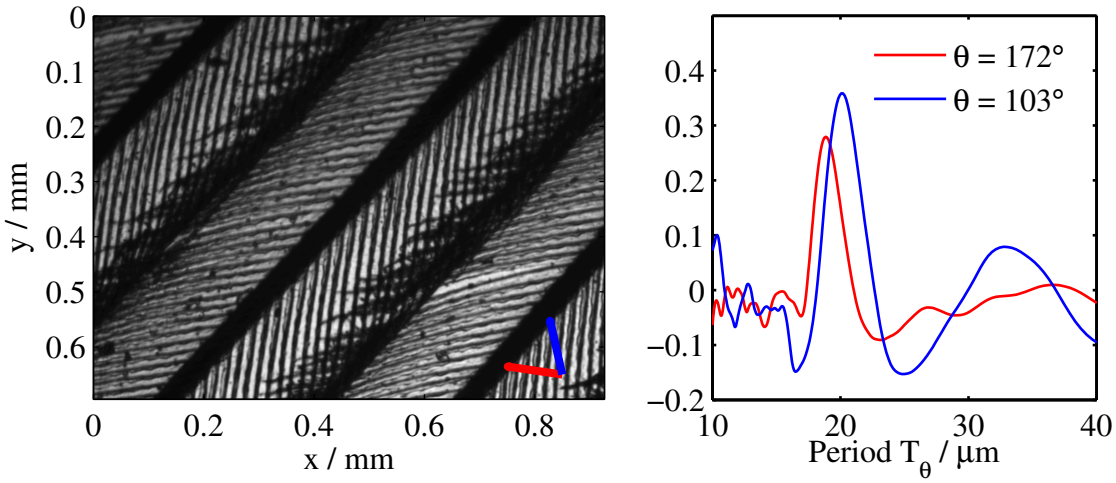

Fig. 5.26. Blackbird feather and corresponding Fourier spectra

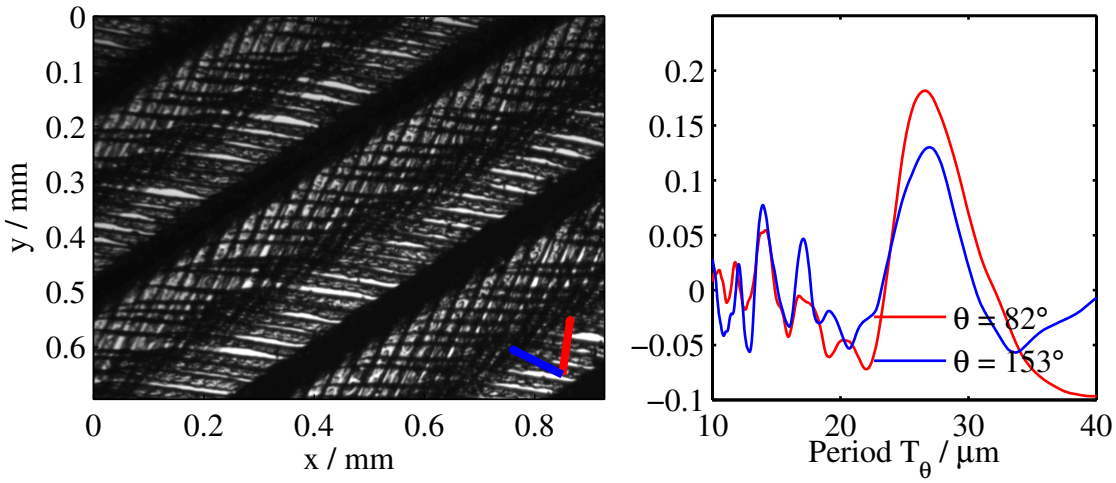

Fig. 5.27. Scarlet bis feather and corresponding Fourier spectra

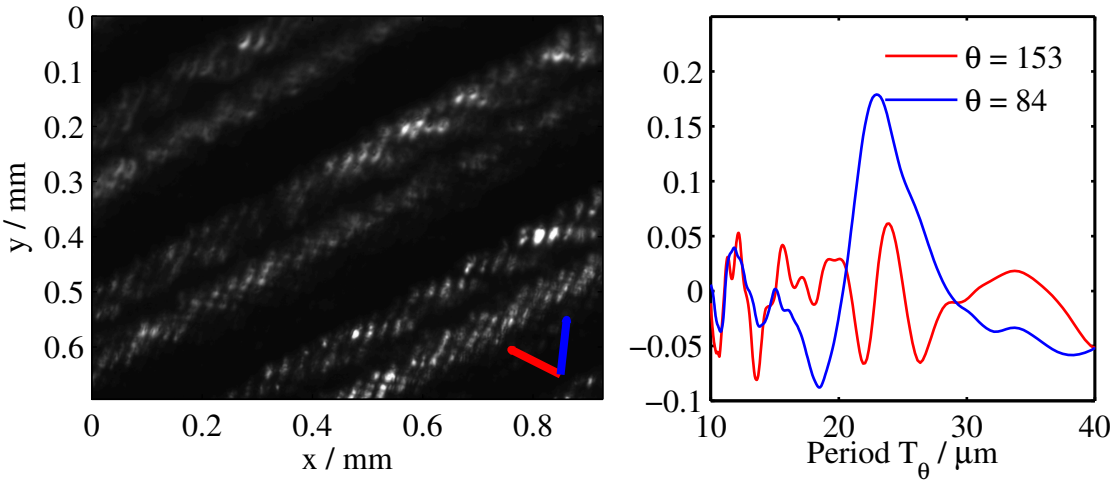

Fig. 5.28. Rook feather and corresponding Fourier spectra

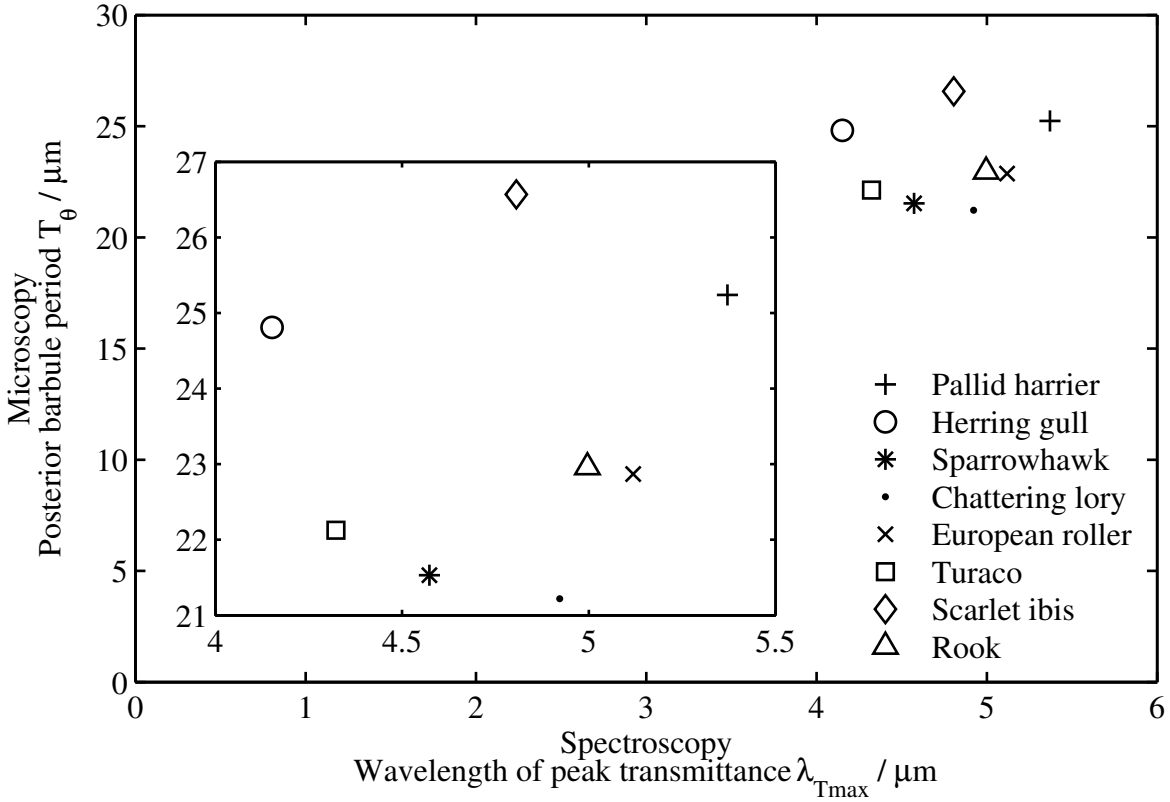

Fig. 5.29. Wavelength of peak transmittance at normal incidence vs. posterior barbule periodicity determined from FTIR measurements and microscope images, respectively. The blackbird feather was excluded since the wavelength of peak transmittance peak could not be determined reliably.

5.3 IR imaging

An example of in-vivo measurement of static birds is shown in Fig. 5.32, taken under laboratory conditions.

In Fig. 5.33 a single frame is shown from the measurements using the TIR setup and dual band telescope, and the ratio between the integrated bands is shown in Fig. 5.34.

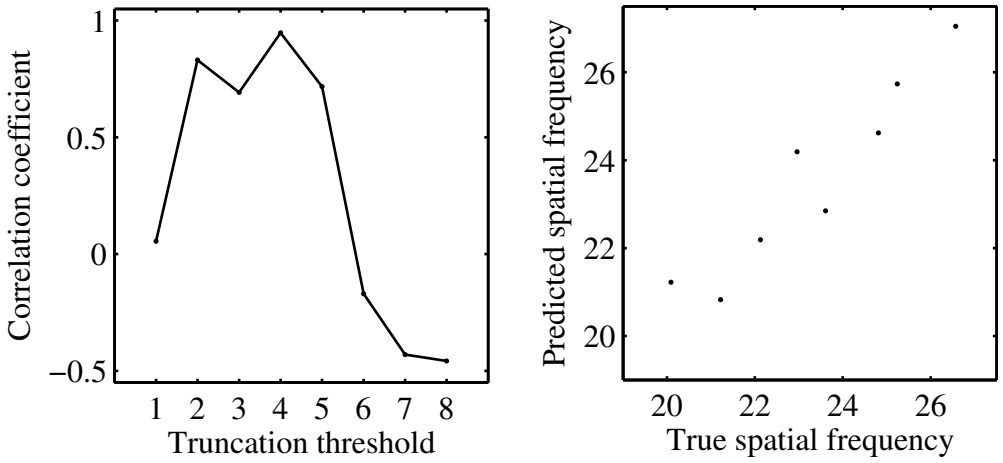

Fig. 5.30. Correlation coefficient between predicted and true barbule spatial periodicities as a function of number of SVD components included in the model (left) and prediction compared to true spatial frequencies (right) when four components were included, and the herring gull feather is excluded.

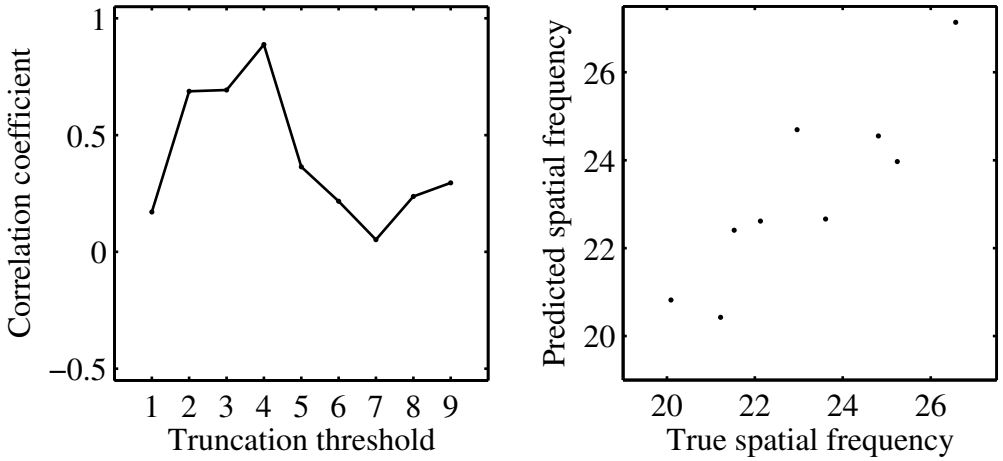

Fig. 5.31. Correlation coefficient between predicted and true barbule spatial periodicities as a function of number of SVD components included in the model (left) and prediction compared to true spatial frequencies (right) when four components were included, with the herring gull feather included in the training data.

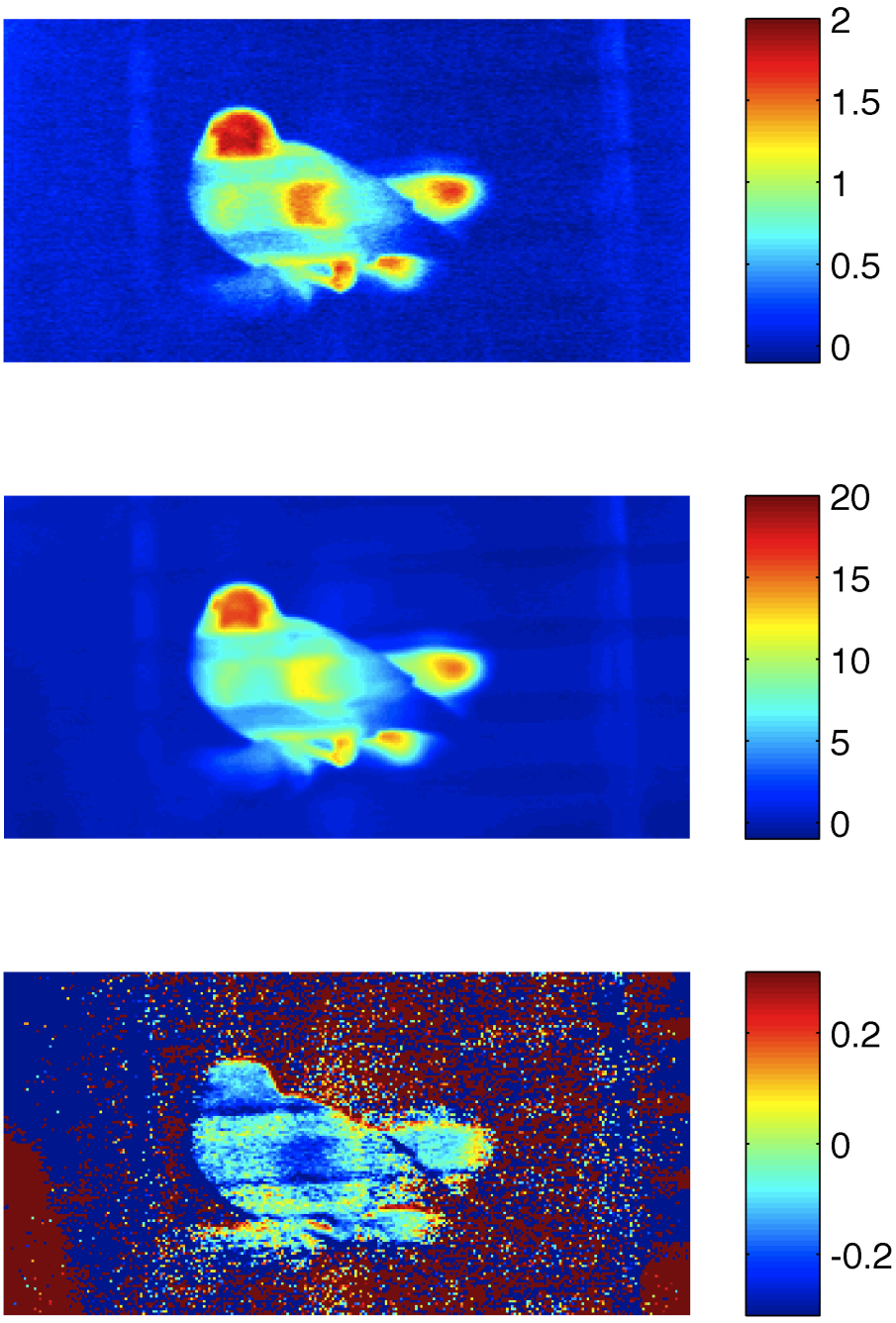

Fig. 5.32. (Note, different color scales.) Top: Image of live Zebra finches in MIR with a fused silica window (I_2); middle: MIR, without filter (I_1); bottom: ratio between the two bands, calculated as $I = (I_1 - 10I_2)/I_1$.

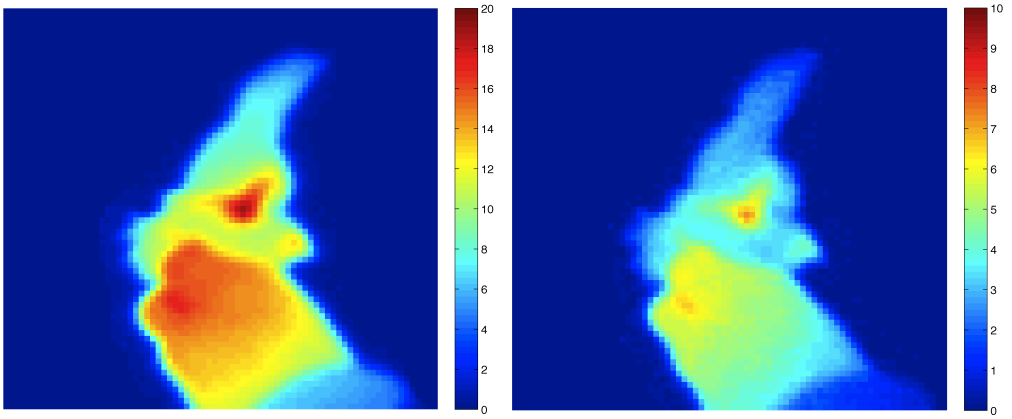

Fig. 5.33. (Note, different color scales.) Images of hand-held Zebra finch in TIR using the dual band telescope after background subtraction, without filter (left) and with a CaF_2 window (right).

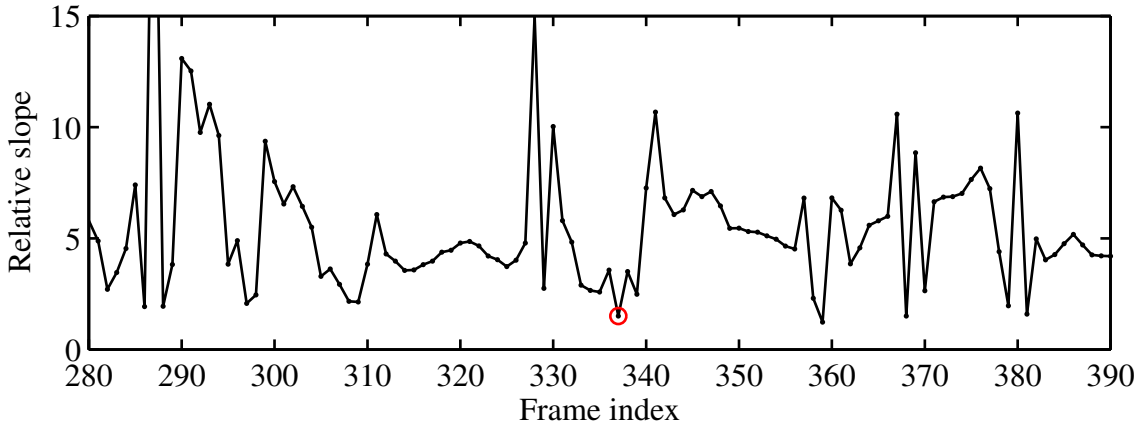

Fig. 5.34. Relative slope I found by integrating over the bird in each TIR band (the indicated frame is depicted in Fig. 5.33; only the top half of the images were integrated), and forming the ratio $I = (I_1 - 2I_2)/I_1$ where I_1 is the integrated signal from the band with no filter present, and I_2 with a CaF_2 window.

Chapter 6

Discussion

6.1 FTIR measurements

In general, the feathers exhibit similar spectral features due to the common β-keratin absorption profile, peaking at 3 µm and having several peaks around 6–7 µm. The smooth baseline in the region 3–6 µm varies considerably between different feathers, and the effect can be seen to extend both to shorter wavelengths and into the TIR, opening up for classification possibilities also inside the atmospheric window between 8–14 µm.

The sharp transmittance peak near $\lambda \approx 5.9$ µm is caused by the Christiansen effect, which occurs when the refractive index of β-keratin coincides with that of air, negating losses at keratin-air interfaces. Since β-keratin absorption peaks at 6 µm, and due to the Kramers-Kronig relations, the refractive index of β-keratin will have a dip at slightly shorter wavelength, causing it to reach 1; cf. Fig. 3.3 on page 11.

At longer wavelengths (between about 15 µm and 25 µm; long end limited by the spectrometer), the transmittance spectrum lacks distinctive features and increases exponentially, which can be explained by that the evanescent wave can no longer be neglected.

A broad peak or distribution in the MIR (3–5 µm) can be seen in most of the spectra, the central wavelength of which shifts according to angle of incidence. The exact dependence becomes more complex by the fact that the shift direction depends on all three axes of rotation, showing similarities to x-ray crystallography. The central position of the peak as a function of angle of incidence lacks symmetry around zero degrees incidence in a lot of cases (herring gull and turaco being the exceptions), and if the observed effects can be described by a thin-film model, the optical surface of the "film" does not coincide with the surface of the feather, which makes sense due to the orientation of the barbules.

Since the transmittance peak shifts when stretching the feather, it can be concluded that the MIR iridescence likely has structural origin and is generated by the air-keratin matrix at a micrometer scale rather than internally as in the visual regime. This is assuming the internal structure of individual barbules or barbs is maintained during stretching. Stretching the

feather about 40 % (mean increase in barbule periodicity may be less than this, however) causes a 7 % shift in wavelength of peak transmittance.

The peak can actually be seen to extend all the way from 2.5 µm to around 10 µm, but the spectrally static features of keratin and the Christiansen effect disrupt the smooth appearance, making exact determination of the peak location difficult, since information is lost in these regions.

The largest variation in the transmittance due to angle of incidence occurs between about 3.5 µm and 5 µm. This coincides with the two atmospheric windows on either side of a CO_2 absorption peak (cf. Fig. 3.1), which is a requirement for remote analysis. Provided the spectral transmittance of feathers from different birds exhibit significantly different angular dependence, remote measurement of the thermal radiation emitted by the bird, spectrally filtered by the wing feathers, in two spectral bands in this region could possibly be used as a means for remote classification. In a field situation, the wing beating of the bird would cause the angle of incidence (or equivalently, angle of observation) of the wing feathers to be modulated in time. For a detector with limited field of view (e.g., the lidar telescope), the time dependence means that a tracking mechanism is required, cf. Fig. 1.1.

To resolve wing beating, the spectral resolution of the Fourier transform spectrometer must be sacrificed for increased temporal resolution. The Nyquist frequency states the absolute limit for strictly sinusoidal signals, but in practice higher sampling frequency is required in order to resolve higher frequency components resulting from a non-harmonic signal. Instead of a spectrometer, an array or scanning detector could to be used, and the spectral bands could be selected either by choice of optical filters, or detector sensitivity, e.g., by selection of band gaps. The first implementation is preferable, since one would not have to take into account any discrepancies in linearity etc. between different detector types. Considering the broad structures involved, filter sharpness is not critical, and various material windows may be used, if suitable materials can be found.

While proving whether the proposed method works for actual live birds cannot be determined by analysis of feathers alone, a few observations can be made. The detector signal S_i for a single spectral band i can be written,

$$S_i = \int_0^\infty S(\lambda, T, \theta)\mathcal{T}_{\text{atm}}(\lambda)D_i(\lambda)\,d\lambda + B_i + R_i(\theta), \tag{6.1}$$

where λ is the wavelength, $S(\lambda, T, \theta)$ is the spectral radiance of the source (the body of the bird) filtered through the plumage, and will thereby depend on the effective body temperature T of the bird, angle of observation θ (see Fig. 1.1), and therefore, wing phase and time. $\mathcal{T}_{\text{atm}}(\lambda)$ is the spectral transmittance of the atmospheric path between bird and detector, and $D_i(\lambda)$

is the combined transmittance of optical filters and detector responsivity, for a given spectral band. The value of B_i includes filter emission and dark current, as well as atmospheric emission, but within an atmospheric window, this is small per definition. Finally, $R_i(\theta)$ describes ambient reflections originating from ground and atmosphere, modified by the reflectance of the plumage of the bird, and is thereby dependent on λ, angle incidence and observation, as well as time. Unless the bird is actively illuminated, R_i is assumed to be small, and will therefore be neglected.

The final value, ultimately used for classification, can be defined by, e.g., the function

$$F = \frac{S_2 - S_1}{S_2 + S_1}, \tag{6.2}$$

where S_1 and S_2 are the signals corresponding to two spectral bands, given by Eq. 6.1. By setting $S(\lambda) = L(\lambda, T)\,\mathcal{T}_{\mathrm{f}}(\lambda)$, with $L(\lambda, T)$ being the spectral radiance of a blackbody at temperature $T = 314\,\mathrm{K}$ and $\mathcal{T}_{\mathrm{f}}(\lambda, \theta)$, experimental filter transmittances from Fig. 4.1 and feather transmittance as a function of angle of incidence θ, and using simulated atmospheric transmittance for $\mathcal{T}_{\mathrm{atm}}(\lambda)$ and detector responsivity from Fig. 4.1, the waveforms in Fig. 6.1 are produced. B_i and R_i have here been set to zero. The resulting waveforms show that at least for single feathers a distinct signal exists that may potentially be used for passive remote sensing in assessing wing beat frequency. In addition, prediction of the angle of incidence may be used for indexing lidar hits in the wing beat cycle. To test whether the waveforms could be used for determination of the angle of incidence or observation, these were analyzed using the SVD, see Fig. 6.2.

Analysis of the thermal radiation emitted by a bird obviously mean that the total signal will be attenuated by filtering through a thick layer of down, but this does not necessarily result in a degradation of the interference effects. Referring to Fig. 6.3, closest to the bird is a skin layer that can be approximated as a graybody radiator. Outside is a thick layer of down, and due to the low photon energies involved, the (macroscopic) scattering due to Fresnel reflections in this region can be expected to be highly inelastic, with the possibility to enhance structural effects in the outer layers; see Fig. 6.3. Due to the inelasticity, Monte Carlo simulation is not a viable alternative, and neither diffusion theory nor Monte Carlo can account for the interference effects. Light transport in tissue is covered in, e.g., [20].

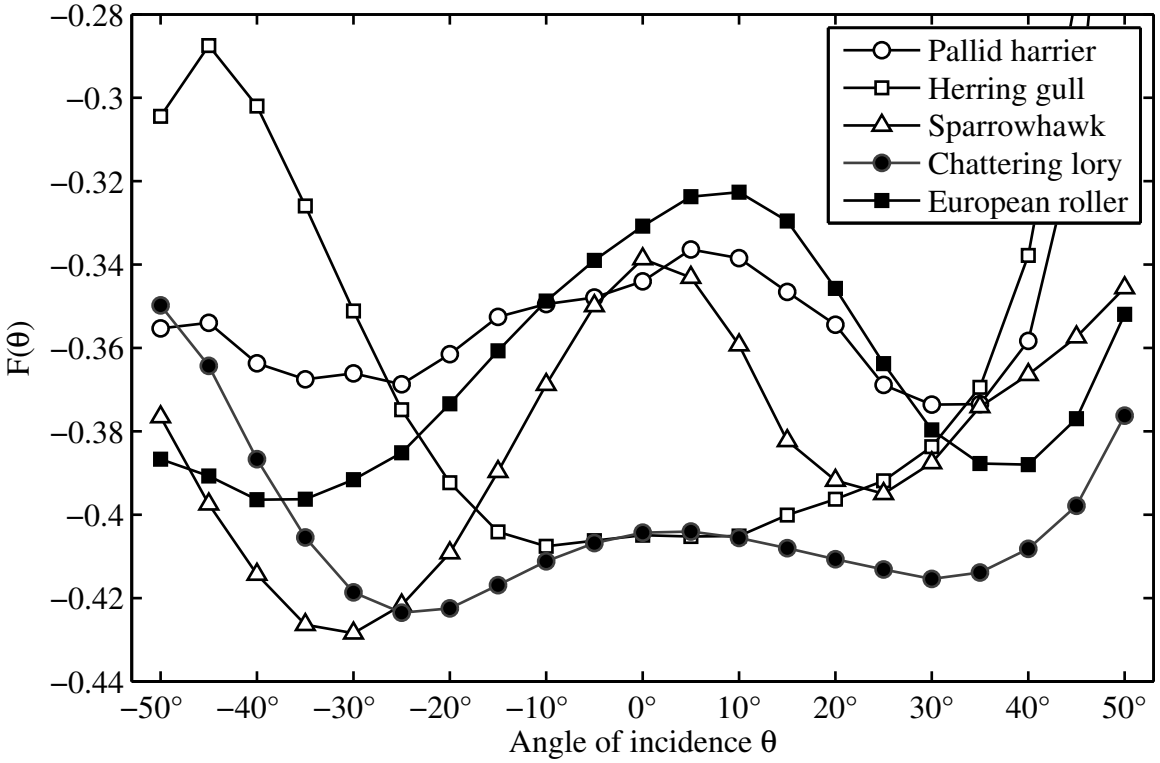

Fig. 6.1. Calculated values for the ratio $F(\theta)$ (given by Eq. 6.2), for experimental feather and filter transmittances, detector responsivity from [18], for a blackbody source at $T = 314\,\mathrm{K}$, as a function of angle of incidence θ to the feather surface, during rotation around the central feather base. Assuming a simple wing model, θ could equivalently be interpreted as the angle of observation of the wing surface relative to the observer, and the waveform would then correspond to one half of a wing beat cycle, as observed from directly below the bird.

6.2 Microscopy and spatial frequency analysis

Barbule periodicities for all feathers falls in the range of about 20–25 µm, but the uncertainty (in half-width sense of the peaks) is of the same order of magnitude, making the estimate of the peak position unreliable. This of course reflects the directional variation of the barbules, and a corresponding broadening of the transmittance spectra can be expected.

The barbule periodicities differ slightly depending on which side of the barb they attach, partly due to their angle to the barb, and the resulting transmittance spectrum can be seen as an average produced by the two sets of barbules. In the case of the chattering lory feather, only anterior barbules

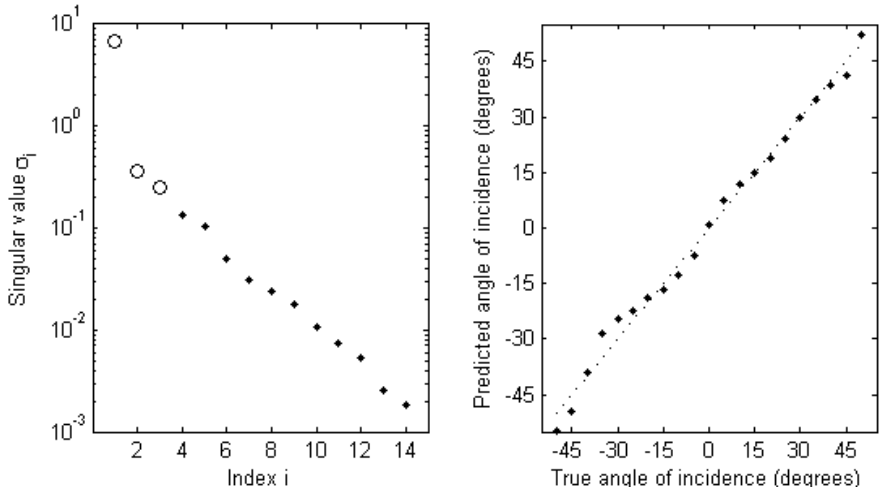

Fig. 6.2. SVD analysis of $F(\theta)$: Singular values (left) and prediction of the angle of incidence $\hat{\theta}$ from the first three principal components, compared to the true angle of incidence θ (right).

overlap, and the transmittance spectrum has rather sharper features in the MIR than the rest, supporting this concept.

No clear correlation exists between the microscopy and spectroscopic measurements, possibly due to uncertainties in both the wavelength of peak transmittance and barbule periodicity due to keratin absorption and Christiansen effect, and variation in orientation of the barbules, respectively. By removing the herring gull the cross validation results could be improved, however.

6.3 IR imaging

While some structure is (barely) visible near the wing in the static ratio image shown (Fig. 5.32), the image is dominated by noise. The conditions are hardly ideal, however, (indoors, slightly below 26 °C ambient temperature), but on the other hand the images are averages of about 50 frames each.

The resulting (TIR) signal shows some modulation due to wing beats (peaks correspond to down-strokes and vice versa), but this may be due to edge-related effects where the bottom-half of the image was cut, resulting in a bias towards one spectral band, and the signal would thus depend on the the relative intensity in each band, i.e., to the cross section of the bird in a given frame.

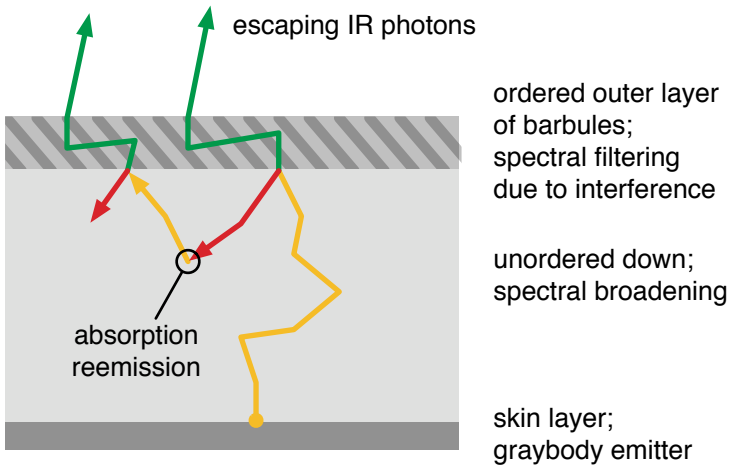

Fig. 6.3. MIR photon migration in bird plumage. A thermal photon absorbed in a small volume element in the down layer will cause the element to experience a slight increase in temperature, leading to a redistribution of the emission spectrum. Due to the spectral transmittance features of the outer layer of feathers, one fraction of the light in the down region will escape, another will be backscattered, absorbed and reemitted with a, statistically, slightly altered wavelength, and will thereby be given another possibility to escape, enhancing the structural effects in the outer layer.

Chapter 7

Conclusions and Future Work

In this thesis, two approaches to night-time bird classification have been explored. Differential optical features in the MIR and TIR have been studied extensively, in order to assess wing-beating patterns of birds, which may ultimately be used for identification. In addition, micrographs of feathers have been analyzed at a microstructure level in order to explain the observed structural MIR colors, possibly opening up for "remote microscopy". The study has identified several difficulties, which is to be expected for a first trial.

In the most trivial case, the oscillation of the thermal signature of a bird due to variation in cross section, caused by wing beating, gives a way of assessing wing-beat frequency, which can be correlated to the body size of the birds. This is essentially what is already being done actively using tracking radar.

Species-dependent information may be gained by additionally observing the ratio between the emitted thermal radiation in two spectral bands in either the MIR or the TIR, spectrally filtered by plumage. For single feathers, the ratio constitutes a waveform under variation of angle of observation, adding a dimension to the trivial modulation depth discussed above. Due to the preferred orientations of the wings, orientations far from parallel in the wing-beat phase will be sampled more frequently, making up for the smaller wing cross section as seen from ground. Due to the symmetry around zero degrees incidence, the signal wings of opposite orientations will aggregate rather than average out. Since the wings constitute a major part of the bird cross section, a fraction of the signal may still survive integration.

A number of feathers were analyzed using frequency analysis for comparison with the MIR spectral features, which may ultimately allow for remote microscopy of bird plumage by interpretation of structural colors. This would require a correlation between a parametrization of the microscope images and knowledge of the spectral features, but as seen, this is not the case. Leaving the herring gull feather out improves the correlation, however. Stretching a feather demonstrates that the barbule periodicity likely is correlated to the spectral transmittance, but other species-related factors not included in the parametrization used for comparison, might also contribute, related to, e.g.,

barbule geometry. A parametrization taking additional parameters, such as the dimension and orientation of the barbules, into account may thus still be able to explain the effects in the MIR. A larger sample set may also improve correlation. Furthermore, correlation may still be expected between groups of individuals, e.g., within a certain geographic location.

A dedicated system for bird detection in the MIR could possibly make use of the existing Lund University lidar telescope. Both MIR detection and lidar would benefit from tracking: a signal sampled at 500 Hz–1 kHz in the MIR could be used either for aiding classification or for determining the phase in the wing beat cycle, and the lidar would also benefit from the increased SNR and the possibility to sample entire wing beats, and thereby the possibility of remote measurement of chromophore concentrations. Tracking could be achieved by splitting off the MIR (or TIR, for increased SNR) light, to a quadrant detector, where the differential signal from opposing detector elements would be used to control the elevational and azimuthal motors of the telescope scanning mirror.

The present study assumes a transmission geometry, where the IR source would constitute the metabolism of the bird, and where the interference effects does not rely on, e.g., collimated radiation. In transmission, the signal will be attenuated by plumage, and the emission at bird body temperature is comparatively low in the MIR. Measurements in reflection mode would not have these limitations. In the field, an OPO could be used as a MIR source. Under laboratory conditions, having a static camera and target guarantees that the same points on the plumage are compared when varying the angle of incident light, which cannot easily be achieved when it is the bird itself that is radiating. The choice of spectral bands could be achieved by sequentially changing filters. Ambient reflections and background could be a problem in the laboratory though, compared to in the field.

A reflection mode would also allow control of the polarization of the illuminating radiation, adding another parameter to the MIR cross section of the bird. The depolarization ratio of bird plumage in the deep UV was investigated in [3]. Due to the ordering of the plumage also at the microstructure level, it can be expected that the MIR depolarization ratio may present another discriminating factor.

Beyond the infrared, for longer wavelengths such as microwaves, matched illumination may be an alternative. A multifrequency system may be utilized similar to how aircraft classification is achieved, where the shape of the target gives rise to a specific signal, due to interference of the backscattered waves [21]; however for birds, as opposed to aircraft, the radar cross section will not only depend on tilt, roll, pitch, incident and observed polarization, and λ, but also on wing phase.

Acknowledgements

My sincere thanks go to my supervisors Mikkel Brydegaard and Sune Svanberg, as well as Patrik Lundin, and the rest of the members of the AMSRS group. In addition, I hereby express my appreciation to the following people and organizations:

Susanne Åkesson and Anna Runemark at the Lund University Department of Animal Ecology, for collaboration in the in-vivo measurements and for general ecology expertise,

The Swedish Research Council and the Kullaberg Foundation, for financial support,

The Lund University Zoological museum for loan of museum specimen,

Jonas Sandsten, for discussions on dual-band IR imaging, and

The Lund University Department of Building Physics, for loan of IR camera.

Permissions for this work on living specimen were given by the Malmö/Lund Ethical Committee for Scientific work on animals (no. M172–06 and M204–06), the Swedish Environmental Protection Agency and the Swedish Ringing Centre.

References

[1] S. A. Gauthreaux, Jr. and J. W. Livingston, "Monitoring bird migration with fixed-beam radar and a thermal-imaging camera," J. Field Ornithol. **77**, 319–328 (2006).

[2] P. Weibring, H. Edner, and S. Svanberg, "Versatile mobile lidar system for environmental monitoring," Appl. Optics **42**, 3583–3594 (2003).

[3] P. Lundin, P. Samuelsson, S. Svanberg, A. Runemark, S. Åkesson, and M. Brydegaard, "Remote nocturnal bird classification by spectroscopy in extended wavelength ranges," (2010). Submitted.

[4] M. Brydegaard, P. Lundin, Z. Guan, A. Runemark, S. Åkesson, and S. Svanberg, "Feasibility study: fluorescence lidar for remote bird classification," Appl. Optics **49**, 4531–4544 (2010).

[5] X. Wan, J. Fan, and H. Wu, "Measurement of thermal radiative properties of penguin down and other fibrous materials using FTIR," Polym. Test. **28**, 673–679 (2009).

[6] Lord Rayleigh (the younger), "The iridescent colours of birds and insects," P. Roy. Soc. Lond. B Bio. **106**, 618–619 (1930).

[7] D. J. Brink and N. G. van der Berg, "Structural colours from the feathers of the bird *Bostrychia hagedash*," J. Phys. D Appl. Phys. **37**, 813–818 (2004).

[8] G. B. Benedek, "Theory of transparency of the eye," Appl. Optics **10**, 459–473 (1971).

[9] R. O. Prum, R. Torres, S. Williamson, and J. Dyck, "Two-dimensional Fourier analysis of the spongy medullary keratin of structurally coloured feather barbs," Proc. R. Soc. Lond. B **266**, 13–22 (1999).

[10] R. O. Prum and R. H. Torres, "A Fourier tool for the analysis of coherent light scattering by bio-optical nanostructures," Integr. Comp. Biol. **43**, 591–602 (2003).

[11] R. O. Prum, J. A. Cole, and R. H. Torres, "Blue integumentary structural colours in dragonflies (*Odonata*) are not produced by incoherent Tyndall scattering," J. Exp. Biol. **207**, 3999–4009 (2004).

[12] E. E. Bell, L. Eisner, J. Young, and R. A. Oetjen, "Spectral radiance of sky and terrain at wavelengths between 1 and 20 microns. ii. Sky measurements," J. Opt. Soc. Am. **50**, 1313–1320 (1960).

[13] V. Lucarini, K.-E. Peiponen, J. J. Saarinen, and E. M. Vartiainen, *Kramers-Kronig Relations in Optical Materials Research* (Springer, Berlin, Heidelberg, 2005).

[14] C. V. Raman, "The theory of the Christiansen experiment," P. Indian A.S. – Math. Sci. **29**, 381–390 (1949).

[15] H. R. Carlon, "Christiansen effect in IR spectra of soil-derived atmospheric dusts," Appl. Optics **18**, 3610–3614 (1979).

[16] M. J. Pollard, P. R. Griffiths, and K. Nishikida, "Investigation of the Christiansen effect in the mid-infrared region for airborne particles," Appl. Spectrosc. **61**, 860–866 (2007).

[17] F. J. Harris, "On the use of windows for harmonic analysis with the discrete Fourier transform," P. IEEE **66** (1978).

[18] A. Rogalski and K. Chrzanowski, "Infrared devices and techniques," Opto-Electron. Rev. **10**, 111–136 (2002).

[19] J. Sandsten, P. Weibring, H. Edner, and S. Svanberg, "Real-time gas-correlation imaging employing thermal background radiation," Opt. Express **6**, 92–103 (2000).

[20] S. L. Jacques and B. W. Pogue, "Tutorial on diffuse light transport," J. Biomed. Opt. **13**, 041302–1–041302–19 (2008).

[21] D. T. Gjessing, J. Hjelmstad, and T. Lund, "A multifrequency adaptive radar for detection and identification of objects: Results on preliminary experiments on aircraft against a sea-clutter background," IEEE T. Antenn. Propag. **AP-30**, 351–365 (1982).